Monthly Notices
of the
ROYAL ASTRONOMICAL SOCIETY

MNRAS **446,** 2802–2822 (2015) doi:10.1093/mnras/stu2278

The role of the artificial conductivity in SPH simulations of galaxy clusters: effects on the ICM properties

V. Biffi[1]⋆ and R. Valdarnini[1,2]

[1]*SISSA – Scuola Internazionale Superiore di Studi Avanzati, Via Bonomea 265, I-34136 Trieste, Italy*
[2]*INFN – Iniziativa Specifica QGSKY, Via Valerio 2, I-34127 Trieste, Italy*

Accepted 2014 October 28. Received 2014 October 15; in original form 2014 July 23

ABSTRACT

We study the thermal structure of the intracluster medium (ICM) in a set of cosmological hydrodynamical cluster simulations performed with a smoothed particle hydrodynamics (SPH) numerical scheme employing an artificial conductivity (AC) term. We explore the effects of this term on the ICM temperature and entropy profiles, thermal distribution, velocity field and expected X-ray emission. We find that in adiabatic runs, the artificial conductivity favours (i) the formation of an entropy core, raising and flattening the central entropy profiles, in better agreement with findings from Eulerian codes; and (ii) a systematic reduction of the cold gas component. In fact, the cluster large-scale structure and dynamical state are preserved across different runs, but the improved gas mixing enabled by the AC term strongly increases the stripping rate of gas from the cold clumps moving through the ICM. This in turn reduces the production of turbulence generated by the instabilities which develop because of the interaction between clumps and ambient ICM. We then find that turbulent motions, enhanced by the time-dependent artificial viscosity scheme we use, are rather damped by the AC term. The ICM synthetic X-ray emission substantially mirrors the changes in its thermodynamical structure, stressing the robustness of the AC impact. All these effects are softened by the introduction of radiative cooling but still present, especially a partial suppression of cold gas. Therefore, not only the physics accounted for, but also the numerical approach itself can have an impact in shaping the ICM thermodynamical structure and ultimately in the use of SPH cluster simulations for cosmological studies.

Key words: methods: numerical – galaxies: clusters: intracluster medium.

1 INTRODUCTION

Within the commonly accepted hierarchical scenario of cosmic structure formation, clusters of galaxies are the latest and largest gravitationally-bound systems formed. For this reason, they most likely still carry the imprints of the underlying cosmological model driving the expansion of the Universe and represent therefore interesting targets for cosmological investigations. During the formation process, baryonic matter, mainly in the form of gas, collapses in the halo potential well shaped by the dominating dark matter (DM) component, cools, fragments and originates the visible structures we observe, such as galaxies (e.g. Kravtsov & Borgani 2012, for a recent review).

Within galaxy clusters, however, the largest fraction of baryons is in the form of diffuse hot plasma – the intracluster medium (ICM) – that emits mainly in the X-rays, with a characteristic temperature which reflects the depth of the cluster potential well. Despite this simplistic description of clusters, observations in several bands (X-ray, radio and optical) have shown pieces of evidence for a more complex thermodynamical structure, characterized for instance by substantial bulk motions, merger-driven shocks, turbulence and cold gas clumps. Processes such as gas cooling, metal diffusion, accretion of pristine gas or smaller haloes, galactic winds, feedback from active galactic nuclei (AGN), interaction between AGN jets and the ambient medium can be sources of non-thermal velocity patterns, local inhomogeneities and hydrodynamical instabilities, that are highly non-linear phenomena.

Hence, an accurate description of clusters through the modelling of such complex physical processes necessarily requires a numerical approach and simulations have indeed proved to be extremely helpful.

Pure *N*-body codes have been extensively studied and tested and are capable of properly follow the formation and evolution of DM-only structures, where gravity is the only force at place. Instead, the numerical treatment of the hydrodynamics still presents some uncertainties, partly reflecting the complexity of the physics involved and partly due to the computational methods themselves.

In the last decades, various of codes have been designed and employed to perform hydrodynamical simulations of both

---

⋆ E-mail: biffi@sissa.it

Published by Oxford University Press on behalf of the Royal Astronomical Society

cosmological volumes and isolated cosmic structures, among which clusters of galaxies. Two different approaches are usually followed: the Lagrangian description is the base for the mesh-free, particle-based smoothed particle hydrodynamics (SPH; Rosswog 2009; Springel 2010a), while the Eulerian grid-based approach is instead employed by adaptive mesh refinement methods (AMR; Berger & Colella 1989; Khokhlov 1998; Norman & Bryan 1999; Fryxell et al. 2000; Teyssier 2002).

Both methods have been widely used to study in a self-consistent manner the hydrodynamics that takes place during the ICM evolution. However, there is now general agreement in the literature that the two numerical methods produce results which differ significantly in a number of hydrodynamical test cases (Agertz et al. 2007; Tasker et al. 2008; Wadsley, Veeravalli & Couchman 2008; Mitchell et al. 2009; Junk et al. 2010; Read, Hayfield & Agertz 2010; Valcke et al. 2010; McNally, Lyra & Passy 2012). In particular, in the SPH approach, the formation of Kelvin–Helmholtz instabilities (KHI) in shear flows is strongly suppressed at the fluid interfaces (Agertz et al. 2007; Read et al. 2010). Moreover, there is a significant discrepancy in the level of core entropy found in simulations of non-radiative clusters performed using the two methods (Wadsley et al. 2008; Mitchell et al. 2009), namely their central entropies are systematically higher by a factor ∼2 in the case of the AMR runs than in the SPH ones. The origin of these differences are due to two distinct causes which significantly affect the standard SPH method. The first problem is the inconsistency of standard SPH in the treatment of contact discontinuities which in turn suppress the growth of KHI at fluid interfaces (Agertz et al. 2007; Price 2008; Read et al. 2010; Valcke et al. 2010). The other difficulty of classic SPH relies in the sampling errors associated with the momentum equation (Inutsuka 2002; Read et al. 2010). This error cannot be reduced by arbitrary increasing the neighbour number, as for the standard SPH cubic spline kernel the onset of clumping instability significantly degrades the convergence rate.

However, the SPH method possesses several properties which render its use particularly appealing in many astrophysical problems. For instance, being the method Lagrangian, it has very good conservation properties and, moreover, is naturally adaptive. For this reason, many authors have recently proposed several improvements in the numerical scheme to solve the problems encountered by standard SPH in handling fluid instabilities (Price 2008; Cha, Inutsuka & Nayakshin 2010; Heß & Springel 2010; Abell 2011; Murante et al. 2011; García-Senz, Cabezón & Escartín 2012; Read & Hayfield 2012; Valdarnini 2012; Power, Read & Hobbs 2014; Saitoh & Makino 2013; Hopkins 2014; Hu et al. 2014). In particular, Price (2008) suggested to include in the SPH thermal energy equation an artificial conduction (AC) term with the purpose of smoothing the thermal energy at fluid interfaces and in turn to ensure a smooth entropy transition at contact discontinuities. A similar term was introduced by Wadsley et al. (2008) with the aim of mimicking the effects of turbulence diffusion, which in SPH is inhibited by the Lagrangian nature of the method. The hydrodynamical performances of this approach were later investigated in detail (Valdarnini 2012), indicating a general improvement over standard SPH in a number of hydrodynamical test problems. In particular, the final levels of core entropies in cosmological simulations of galaxy clusters were found consistent with those found using AMR codes. This result is in accord with previous studies (Wadsley et al. 2008; Mitchell et al. 2009), showing that in standard SPH it is the lack of diffusion and the subsequent damping of entropy mixing which are responsible for the differences in central entropies between AMR and SPH galaxy cluster simulations.

Motivated by these findings, we investigate here the impact of the new AC-SPH scheme on the ICM thermodynamical properties of a set of simulated galaxy clusters. The baseline sample consists of eight different initial conditions for the simulated clusters, extracted from a larger cosmological ensemble. We construct an ensemble of different test cases by performing, for the same set of initial conditions, simulations with different settings in the hydrodynamical part of the code. The code implements a time-dependent artificial viscosity (AV) scheme, and we consider runs with different AV parameters as well as simulations which incorporate or not the AC term. In addition, we consider both non-radiative simulations and runs in which the gas can cool radiatively.

The principal aim of this investigation is to study in detail how the proposed hydrodynamical scheme modifies the thermodynamic of the ICM and in turn its impact on cluster X-ray observational properties.

The paper is organized as follows. In Section 2, we introduce the main hydrodynamical modifications of the SPH scheme used to run the various simulations, and the construction of the sample of simulated clusters is then described in Section 3. In Section 4, we provide the statistical tools used to explore the dynamical state of the clusters, in terms of morphology and gas velocity field. Results on how the numerical improvements of SPH impact the final ICM thermodynamical properties are presented and extensively discussed in Section 5. Finally, we summarize our findings and draw our conclusions in Section 7.

2 SIMULATIONS

We now outline here the fundamentals of the hydrodynamical method – we refer the reader to Rosswog (2009) and Price (2012a), for comprehensive reviews.

2.1 Basic equations

According to the SPH method, the fluid is described by a set of particles with mass m_i, velocity $\boldsymbol{v}_i$, density ρ_i, thermal energy per unit mass u_i and entropy A_i. The latter is related to the particle pressure P_i by $P_i = A_i\rho_i^\gamma = (\gamma - 1)\rho_i u_i$, where $\gamma = 5/3$ for a mono-atomic gas. The density at the particle position $\boldsymbol{r}_i$ is given by

$$\rho_i = \sum_j m_j W(|\boldsymbol{r}_{ij}|, h_i), \tag{1}$$

where $W(|\boldsymbol{r}_i - \boldsymbol{r}_j|, h_i)$ is the cubic spline kernel that has compact support and is zero for $|\boldsymbol{r}_i - \boldsymbol{r}_j| \geq 2h_i$ (Price 2012a). The sum in equation (1) is over a finite number of particles and the smoothing length h_i is a variable that is implicitly determined by

$$h_i = \eta(m_i/\rho_i)^{1/D}, \tag{2}$$

so that for the adopted spline $N_{\rm sph} = 4\pi\rho_i(2h_i)^3/3 = 4\pi(2\eta)^3/3$ is the number of neighbouring particles of particle i within a radius $2h_i$. The Euler equation can be derived by a Lagrangian formulation (Rosswog 2009; Price 2012a):

$$\frac{\mathrm{d}\boldsymbol{v}_i}{\mathrm{d}t} = -\sum_j m_j \left[\frac{P_i}{\Omega_i\rho_i^2}\nabla_i W_{ij}(h_i) + \frac{P_j}{\Omega_j\rho_j^2}\nabla_i W_{ij}(h_j)\right], \tag{3}$$

with the coefficients Ω_i being given by

$$\Omega_i = \left[1 - \frac{\partial h_i}{\partial \rho_i}\sum_k m_k \frac{\partial W_{ik}(h_i)}{\partial h_i}\right]. \tag{4}$$

To properly treat the effects of shocks, the term in the rhs of equation (3) must be complemented by the viscous force

$$\left(\frac{\mathrm{d}\boldsymbol{v}_i}{\mathrm{d}t}\right)_{\mathrm{AV}} = -\sum_i m_j \Pi_{ij} \nabla_i \bar{W}_{ij}, \tag{5}$$

where the term $\bar{W}_{ij} = \frac{1}{2}(W(r_{ij}, h_i) + W(r_{ij}, h_j))$ is the symmetrized kernel and Π_{ij} is the AV tensor.

Following Monaghan (1997), the latter is written as

$$\Pi_{ij} = -\frac{\alpha_{ij}}{2}\frac{v_{ij}^{\mathrm{AV}}\mu_{ij}}{\rho_{ij}} f_{ij}, \tag{6}$$

where a pair of subscripts denotes arithmetic averages, and the signal velocity v_{ij}^{AV} is given by

$$v_{ij}^{\mathrm{AV}} = c_i + c_j - 3\mu_{ij}, \tag{7}$$

with c_i being the sound velocity, $\mu_{ij} = \boldsymbol{v}_{ij} \cdot \boldsymbol{r}_{ij}/|r_{ij}|$ if $\boldsymbol{v}_{ij} \cdot \boldsymbol{r}_{ij} < 0$ but zero otherwise and $\boldsymbol{v}_{ij} = \boldsymbol{v}_i - \boldsymbol{v}_j$. The parameter α_i regulates the amount of AV, and f_i is a damping factor which is introduced to reduce the strength of AV when shear flows are present. For this term, Balsara (1995) proposed the expression

$$f_i = \frac{|\nabla \cdot \boldsymbol{v}|_i}{|\nabla \cdot \boldsymbol{v}|_i + |\nabla \times \boldsymbol{v}|_i}, \tag{8}$$

where $(\nabla \cdot \boldsymbol{v})_i$ and $(\nabla \times \boldsymbol{v})_i$ are the standard SPH estimates for divergence and curl.

For the viscosity parameter α_i, it is assumed $\alpha_i = \text{constant} \equiv \alpha_0 = 1$, in standard SPH, whilst Morris & Monaghan (1997) suggested to let the parameter to vary with time so that the strength of the AV is reduced away from shocks. In such a case, the time evolution of α_i is given by

$$\frac{\mathrm{d}\alpha_i}{\mathrm{d}t} = -\frac{\alpha_i - \alpha_{\mathrm{min}}}{\tau_i} + S_i, \tag{9}$$

where

$$\tau_i = \frac{h_i}{c_i\, l_{\mathrm{d}}} \tag{10}$$

is a decay time-scale which is controlled by the dimensionless decay parameter l_{d}, α_{min} is a floor value and S_i is a source term. This is constructed so that it increases in the presence of shocks:

$$S_i = f_i S_0 \max(-(\nabla \cdot \boldsymbol{v})_i, 0)(\alpha_{\mathrm{max}} - \alpha_i) \equiv \mathcal{S}_i(\alpha_{\mathrm{max}} - \alpha_i). \tag{11}$$

Here, S_0 is unity for $\gamma = 5/3$. Recommended values for the parameters α_{max}, α_{min} and l_{d} are 1.5, 0.05 and 0.2, respectively (Rosswog 2009). In principle, one can reduce the presence of AV by decreasing τ_i as much as possible. None the less, a lower limit to the time-scale τ_i is set by the minimum time taken to propagate through the resolution length h_i, so that the value $l_{\mathrm{d}} = 1$ sets an upper limit to the parameter l_{d}.

For mild or weak shocks and very short decaying time-scales, the peak value of α_i at the shock front might be however below the value necessary to avoid inconsistencies in the integration. In order to maintain the same shock resolution capabilities when $l_{\mathrm{d}} \geq 0.2$, a prefactor ξ is introduced in equation (11) by substituting α_{max} with $\alpha_{\mathrm{max}} \to \xi\alpha_{\mathrm{max}}$ (Valdarnini 2011, hereafter V11). The correction factor ξ was calibrated in a number of hydrodynamical tests, obtaining $\xi = (l_{\mathrm{d}}/0.2)^{0.8}$ for $l_{\mathrm{d}} \geq 0.2$ (V11).

In the following, simulation runs performed according to the standard AV scheme will be denoted by AV_0, whereas the labels AV_2 and AV_5 will indicate simulations employing a time-dependent AV scheme with parameters $\{\alpha_{\mathrm{min}}, \alpha_{\mathrm{max}}, l_{\mathrm{d}}\} = \{0.1, 1.5, 0.2\}$ and $\{0.01, 1.5, 1\}$, respectively.

For the number of neighbours N_{sph}, typical values lie in the range $N_{\mathrm{sph}} \sim 33$–50, here we use $N_{\mathrm{sph}} = 33 (\eta \sim 1.06)$. Setting $N_{\mathrm{sph}} = 64$ would have improved the accuracy in density estimates below a few per cent (see table 3 of Valdarnini 2012) at the price of doubling the computational cost of SPH summations.

2.2 The artificial conductivity scheme

In the SPH code we use, we also adopt an entropy-conserving approach (Springel & Hernquist 2002), in which entropy is generated at a rate

$$\frac{\mathrm{d}A_i}{\mathrm{d}t} = \frac{\gamma - 1}{\rho_i^{\gamma-1}}\{Q_{\mathrm{AV}} + Q_{\mathrm{R}} + Q_{\mathrm{AC}}\}, \tag{12}$$

where the terms in brackets refer to different sources. In particular, Q_{AV} is the source term due to viscosity:

$$Q_{\mathrm{AV}} = \left(\frac{\mathrm{d}u_i}{\mathrm{d}t}\right)_{\mathrm{AV}} = \frac{1}{2}\sum_j m_j \Pi_{ij} \boldsymbol{v}_{ij} \cdot \nabla_i \bar{W}_{ij}. \tag{13}$$

The term Q_{AC} in equation (12) represents an artificial conduction term and has been introduced by Price (2008) with the purpose of avoiding inconsistencies in the treatment of thermal energy at contact discontinuities. This term can be written as

$$\left(\frac{\mathrm{d}u_i}{\mathrm{d}t}\right)_{\mathrm{AC}} = \sum_j \frac{m_j v_{ij}^{\mathrm{AC}}}{\rho_{ij}} \left[\alpha_{ij}^C (u_i - u_j)\right] \boldsymbol{e}_{ij} \cdot \nabla_i \bar{W}_{ij}, \tag{14}$$

where v_{ij}^{AC} is the signal velocity, $\boldsymbol{e}_{ij} \equiv \boldsymbol{r}_{ij}/r_{ij}$, and α_i^C is the AC parameter. In analogy with the AV scheme, the AC parameter evolves in time according to

$$\frac{\mathrm{d}\alpha_i^C}{\mathrm{d}t} = -\frac{\alpha_i^C - \alpha_{\mathrm{min}}^C}{\tau_i^C} + S^C{}_i, \tag{15}$$

where $\tau_i^C = h_i/0.2c_i$, and the source term is given by

$$S^C{}_i = f_C h_i \frac{|\nabla^2 u_i|}{\sqrt{u_i + \varepsilon}} \left(\alpha_{\mathrm{max}}^C - \alpha_i^C\right). \tag{16}$$

Here, the Laplacian is calculated according to

$$\nabla^2 u_i = 2 \sum_j m_j \frac{u_i - u_j}{\rho_j} \frac{\boldsymbol{e}_{ij} \cdot \nabla W_{ij}}{r_{ij}}. \tag{17}$$

In what follows, we set $f_C = 1$, $\alpha_{\mathrm{min}}^C = 0$ and $\alpha_{\mathrm{max}}^C = 1.5$, $\varepsilon = 10^{-4} u_i$. For the signal velocity, we use

$$v_{ij}^{\mathrm{AC}} = |(\boldsymbol{v}_i - \boldsymbol{v}_j) \cdot \boldsymbol{r}_{ij}|/r_{ij}. \tag{18}$$

This choice guarantees the absence of thermal diffusion for self-gravitating systems in hydrostatic equilibrium and its reliability has been tested in a number of hydrodynamical tests (Valdarnini 2012) in which gravity is present.

Finally, for the cooling runs, the term $Q_{\mathrm{R}} = -\Lambda(\rho_i, T_i)$ – T_i being the particle temperature – accounts for the radiative losses. For these simulations, the physical modelling of the gas includes radiative cooling, star formation, energy feedback and metal enrichment that follow from supernova explosions (see Valdarnini 2006, for a detailed description of the implemented procedures).

The code including the AC modification will be also referred to as AC-SPH, in the following.

3 SAMPLE CONSTRUCTION

To construct our ensemble of hydrodynamical cluster simulations, we use a baseline sample consisting of eight different initial

Table 1. Main cluster properties and simulation parameters of the considered sample. From left to the right: parent cosmological sample, cluster id, cluster mass M_{200} (within R_{200}) in units of $h^{-1}\,\mathrm{M}_{\odot}$, cluster radius R_{200} is units of Mpc, number of gas (N_{gas}) and dark matter (N_{DM}) particles inside the initial high-resolution sphere, mass of the gas (m_{gas}) and dark matter (m_{DM}) particles in $\mathrm{M}_{\odot}$, gravitational softening parameter for the gas in kpc.

Sample	Index	$M_{200}(h^{-1}\,\mathrm{M}_{\odot})$	R_{200} (Mpc)	N_{gas}	N_{DM}	$m_{\mathrm{gas}}(\mathrm{M}_{\odot})$	$m_{\mathrm{DM}}(\mathrm{M}_{\odot})$	$\varepsilon_{\mathrm{gas}}$ (kpc)
S_8	1	6×10^{14}	1.96	220 175	220 144	3×10^{9}	1.5×10^{10}	25.4
S_4	5	2.4×10^{14}	1.45	221 007	220 976	2×10^{9}	1.1×10^{10}	22.2
S_4	11	5.7×10^{14}	1.94	220 759	220 728	1.5×10^{9}	7.6×10^{9}	20
S_4	16	2×10^{14}	1.37	221 167	221 136	1.7×10^{9}	8.7×10^{9}	21
S_4	19	7×10^{14}	2.07	219 631	219 600	1.7×10^{9}	8.7×10^{9}	21
S_2	13	2.4×10^{14}	1.44	221 823	221 792	6.4×10^{8}	3.3×10^{9}	15.1
S_2	105	6×10^{13}	0.91	221 391	221 360	2.5×10^{8}	1.3×10^{9}	11.1
S_2	110	9.4×10^{13}	1.05	222 111	222 080	2.5×10^{8}	1.3×10^{9}	11.1

conditions for the simulated clusters. These objects have been extracted from a set of cosmological simulations, for which we assume a standard Λ cold dark matter cosmological model with present matter density $\Omega_{\mathrm{m}} = 0.3$, cosmological constant density parameter $\Omega_{\Lambda} = 0.7$, baryonic density $\Omega_{\mathrm{b}} = 0.0486$, power spectrum normalization $\sigma_8 = 0.9$, primeval power spectrum index $n = 1$ and Hubble constant $H_0 = 70 \equiv 100h\,\mathrm{km\,s^{-1}\,Mpc^{-1}}$.

In order to construct the cluster subsample, we first run a DM only simulation with comoving box size $L_2 = 200h^{-1}$ Mpc. The DM haloes are then identified at $z = 0$ using a friends-of-friends algorithm, so as to detect overdensities in excess of $\sim 200\Omega_{\mathrm{m}}^{-0.6}$ within a radius R_{200}. The corresponding mass is defined as M_{200}, where

$$M_{\Delta} = (4\pi/3)\,\Delta\,\rho_{\mathrm{c}}\,R_{\Delta}^{3} \tag{19}$$

denotes the mass contained in a sphere of radius R_{Δ} with mean density Δ times the critical density ρ_{c}.

The haloes are then sorted according to the value of their mass M_{200} to generate a catalogue of $N_2 = 120$ simulated clusters, which have been then re-simulated individually using both the standard and the entropy-conserving AC-SPH code described in Section 2. The re-simulations were performed using a zoom-in method (see V11 for more details) so that at the initial redshift each cluster comprises $\sim$220 000 gas and DM particles within a sphere of comoving radius $\propto R_{200}$. The gravitational softening parameter of the particles is set according to the scaling $\varepsilon_i \propto m_i^{1/3}$, where m_i is the mass of particle i. The relation is normalized by $\varepsilon_i = 15(m_i/6.2 \times 10^{8}\,\mathrm{M}_{\odot})^{1/3}$ kpc. The set of simulated clusters constructed in this way is referred to as sample S_2.

With a similar procedure, we generate the cluster samples S_4 and S_8, from cosmological simulations with box sizes $L_4 = 400\,h^{-1}$ Mpc and $L_8 = 800h^{-1}$ Mpc. The S_8 and S_4 sets consist of $N_8 = 10$ and $N_4 = 33$ clusters, respectively, and have been constructed such that the threshold in mass for the S_4 haloes is greater than the maximum M_{200} mass of the S_2 sample, and a similar criterion holds for S_8, with respect to S_4. The final catalogue (S_{all}) is built combining the three aforementioned ones.

The eight clusters, whose initial conditions are used for the present analysis, have been finally selected as a representative subsample of the mass range and dynamical states of the whole set S_{all} (similarly to V11).

The main properties of these clusters are reported in Table 1.

4 STATISTICAL TOOLS

In this section, we describe the statistical tools used to measure the cluster morphology and the spectral properties of the ICM velocity field. The former is quantified using the power ratios and the centroid shifts of the simulated cluster, whereas the longitudinal and solenoidal components of the velocity power spectrum are analysed separately to obtain statistical measurements of the ICM velocity field. The implementation of the spectral analysis is the same as in V11, to which we refer for more details.

4.1 Indicators of the cluster dynamical state

We quantify the dynamical state of the simulated clusters using two methods: the power ratio (Buote & Tsai 1995) and the centroid shift (Mohr, Fabricant & Geller 1993; O'Hara et al. 2006). In the power-ratio method, the projected X-ray surface brightness $\Sigma_{\mathrm{X}}(\boldsymbol{x})$ is the source term of the pseudo-potential $\Psi(\boldsymbol{x})$ which satisfies the 2D Poisson equation. A multipole expansion of the solution gives the moments

$$\alpha_{\mathrm{m}} = \int_{R' \leq R} \mathrm{d}^2x'\,\Sigma_{\mathrm{X}}(\boldsymbol{x}')R'^{\mathrm{m}}\cos(\mathrm{m}\varphi') \tag{20}$$

and

$$\beta_{\mathrm{m}} = \int_{R' \leq R} \mathrm{d}^2x'\,\Sigma_{\mathrm{X}}(\boldsymbol{x}')R'^{m}\sin(\mathrm{m}\varphi'), \tag{21}$$

where the integral extends over a circular aperture of radius $R \equiv R_{\mathrm{ap}}$ (i.e. the aperture radius). Then, the power ratios are defined according to

$$\Pi^{(\mathrm{m})}(R_{\mathrm{ap}}) = \log_{10}(P_{\mathrm{m}}/P_0), \tag{22}$$

where

$$P_{\mathrm{m}}(R_{\mathrm{ap}}) = \frac{1}{2\,m^2}(\alpha_{\mathrm{m}}^2 + \beta_{\mathrm{m}}^2)m > 0, \tag{23}$$

$$P_0 = [\alpha_0 \ln(R_{\mathrm{ap}}/\mathrm{kpc})]^2. \tag{24}$$

In the following, we will use the quantity $\Pi_3(R_{\mathrm{ap}})$ as an indicator of the cluster dynamical state, since it provides an unambiguous detection of asymmetric structure. Moreover, we minimize projection effects by introducing the average quantity $\bar{\Pi}_3(R_{\mathrm{ap}}) = \log_{10}(\bar{P}_3/\bar{P}_0)$, where $\bar{P}_{\mathrm{m}}$ is the *rms* average of the moments P_{m} evaluated along the three orthogonal lines of sight (l.o.s.).

Another useful measure commonly employed to quantify cluster morphology is the centroid shift. This method is based on the displacement between the cluster centre and the centroid calculated using the first moment of the X-ray surface brightness. Following Böhringer et al. (2010), we then calculate the centroids within nine apertures with radii $r = 0.1 \times i \times R_{\mathrm{ap}}$, with $i = 2, 3, \ldots, 10$. We excise from the computation a central region of radius $r = 0.05R_{\mathrm{ap}}$.

The centroid shift is then defined as the standard deviation of the centroids in units of R_{500}:

$$w = \left[\frac{1}{N-1}\sum(\Delta_i - <\Delta>)\right]^{1/2} \times \frac{1}{R_{500}}, \qquad (25)$$

where Δ_i is the centroid corresponding to the ith aperture.

For the present analysis, we evaluate both power ratios and centroid shifts for the regions enclosed within three typical aperture radii: $R_{\rm ap} = R_{2500}$, R_{500} and R_{200}.

To compute the centroid shift, a common choice for the coordinate origin is the X-ray peak of the surface brightness. However, for the numerical study undertaken here, this choice is not free of possible ambiguities. Because of the presence of the new AC term in the thermal energy equation, there might be significant variations in the final gas thermal properties between simulations performed for the same test cluster, depending on whether the AC term is included or not. This in turn might imply variations in the location of the gas emission peak between different runs and a difficulty to consistently compare quantities for which their definition depends on the choice of the origin.

In order to avoid this difficulty and to unambiguously identify the same emission peak among different runs, we have used the following procedure to determine the cluster centre. The latter is defined as the maximum of the gas density, calculated iteratively as the centre of mass of the gas particles contained within spheres of shrinking radius (Valdarnini 2006). However, the origin of the first sphere is located at the maximum of the DM density, which is determined using the same approach.

We found this procedure to produce quite stable cluster centre identifications, thereby allowing to unambiguously compare results from different runs. The cluster centre defined in this way is consistently used also in the computation of the power ratios as well as in that of spherically averaged radial profiles of several hydrodynamic variables. Finally, to remove cold clumps from the computation of the power ratios and centroid shifts, we consider only gas particles with temperatures above 0.5 keV.

4.2 Velocity-field diagnostics

The spectral properties of the ICM velocity field are quantified using the velocity power spectrum $E(k)$. This is computed by first determining $\boldsymbol{u}_w{}^d(\boldsymbol{k})$, the discrete Fourier transform of the density-weighted velocity field $\boldsymbol{u}_w(\boldsymbol{x}) \equiv w(\boldsymbol{x})\boldsymbol{u}(\boldsymbol{x})$, where $w(\boldsymbol{x}) \propto \rho(x)^{1/2}$.

To obtain the transform $\boldsymbol{u}_w{}^d(\boldsymbol{k})$, a cube of size $L_{\rm sp} = R_{200}$ with $N_{\rm g}^3 = 128^3$ grid points is placed at the cluster centre and the velocity field is computed at the grid points $\boldsymbol{x}_p$ according to the SPH prescription. The discrete transforms of $\boldsymbol{u}_w(\boldsymbol{x}_p)$ are then found using fast Fourier transforms and used to define a dimensionless velocity power spectrum

$$E(k) = \frac{1}{L_{\rm sp}\sigma_v^2}\left[2\pi k^2 \mathcal{P}^{\rm d}(k)\left(\frac{L_{\rm sp}}{2\pi}\right)^3\right], \qquad (26)$$

where $\sigma_v = \sqrt{GM_{200}/r_{200}}$, $k = |\boldsymbol{k}|$ and $\mathcal{P}^{\rm d}(k) =< |\boldsymbol{u}_w{}^d(\boldsymbol{k})|^2$ is the spherically averaged discrete power spectrum.

In addition, we address separately the longitudinal and solenoidal components of the power spectrum by introducing in the $\boldsymbol{k}$-space the corresponding velocity field components

$$\boldsymbol{u}(\boldsymbol{k})_{\rm shear} = \frac{\boldsymbol{k} \times \boldsymbol{u}(\boldsymbol{k})}{|\boldsymbol{k}|}, \qquad (27)$$

$$\boldsymbol{u}(\boldsymbol{k})_{\rm comp} = \frac{\boldsymbol{k} \cdot \boldsymbol{u}(\boldsymbol{k})}{|\boldsymbol{k}|}. \qquad (28)$$

The velocity power spectrum is then defined as $E(k) = E_s(k) + E_c(k)$ (Kitsionas et al. 2009).

5 RESULTS

In this section, we present and discuss the main results of our analysis. The notation that will be adopted to distinguish the various simulation runs can be sketched as follows:

(i) depending on the physics included in the simulations, 'ar' will refer to adiabatic runs, 'cr' will refer to radiative runs (comprising cooling, star formation and metal production);

(ii) depending on the particular modification of the viscosity scheme (AV$_2$, AV$_5$; see Section 2), we will refer to the adiabatic runs as 'ar2, ar5' and to the radiative runs as 'cr2, cr5';

(iii) 'ar0' and 'cr0' runs will be always used as terms of comparison, being the reference simulations with standard SPH and fixed viscosity (NOAC, AV$_0$); for the other runs, instead, we consider both the standard SPH version (NOAC) and the modification including the artificial conductivity term (AC).

5.1 Adiabatic runs

Here, we discuss the results on radial and global properties of the simulated clusters, for different adiabatic runs at redshift $z = 0$. Differences in the simulations consist in the modifications to the classical SPH approach presented in Sections 2 and 2.2. In this section, we consider as reference case the adiabatic run: 'ar0' (NOAC, AV$_0$).

5.1.1 Entropy and temperature profiles

We explore the different properties of the ICM in the adiabatic runs by investigating the spherically-averaged radial entropy and temperature profiles of the sample clusters, as shown in Figs 1 and 2. In order to allow for a fair comparison among different clusters, the profiles are shown as a function of r/R_{200}. The temperature profiles are expressed in units of T_{200}, and employ the mass-weighted temperature, which represents the 'dynamical' temperature of the gas, without any bias due to its thermal phase (e.g. emissivity). For the entropy profiles, we rescale the values to

$$S_{200} = \frac{1}{2}\left[\frac{2\pi}{15}\frac{G^2 M_{200}}{f_{\rm b} H_0}\right]^{2/3}, \qquad (29)$$

where $f_{\rm b} = \Omega_{\rm b}/\Omega_{\rm m}$ is the global baryon fraction.

Despite the different configurations of individual objects, the results in Figs 1 and 2 indicate that the introduction of the AC term (coloured, dashed curves in the plots) tends in general to produce cluster cores with higher entropy and higher temperature with respect to their standard-SPH counterparts (NOAC; coloured, solid lines). The AC term basically facilitates the redistribution of internal energy produced in shocks and enhances the entropy mixing, thereby increasing the entropy level in the core. The major differences between AC and NOAC entropy profiles – up to a factor of ~4 – are in fact visible at $r/R_{200} < 0.1$, whereas there is reasonable agreement at larger distances from the centre. In some individual cases, the entropy profile even presents a real plateau towards the cluster centre, approaching the features obtained by AMR codes and observed in real clusters. Temperature profiles (right-hand column

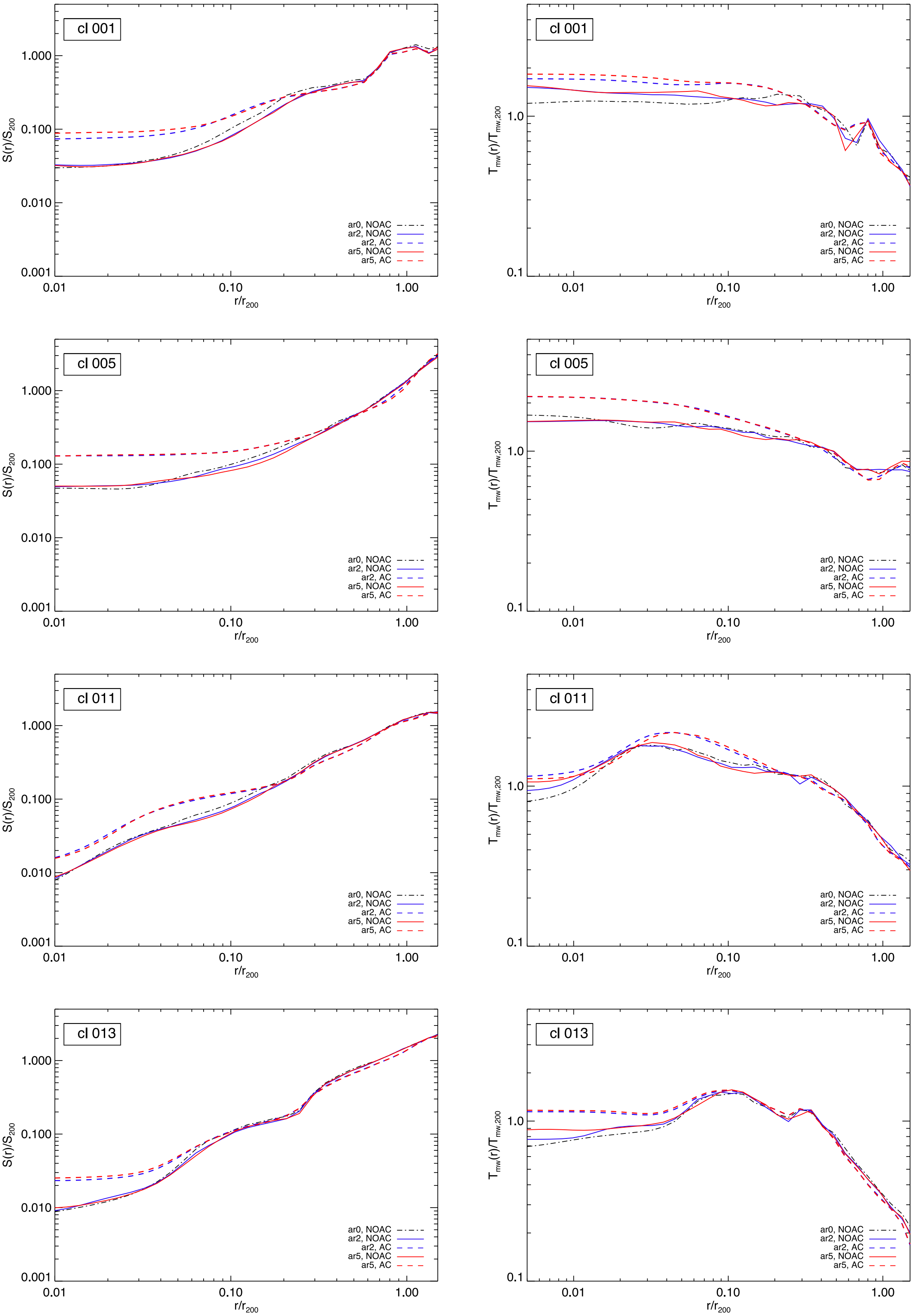

Figure 1. Entropy and temperature profiles of the clusters in the sample, for the adiabatic simulations at $z = 0$. Different lines refer to different runs: AC-SPH (dashed) and standard SPH (solid), for the two viscosity schemes AV$_2$ (blue) and AV$_2$ (red). The dot–dashed black line marks the reference run (ar0; NOAC – AV$_0$).

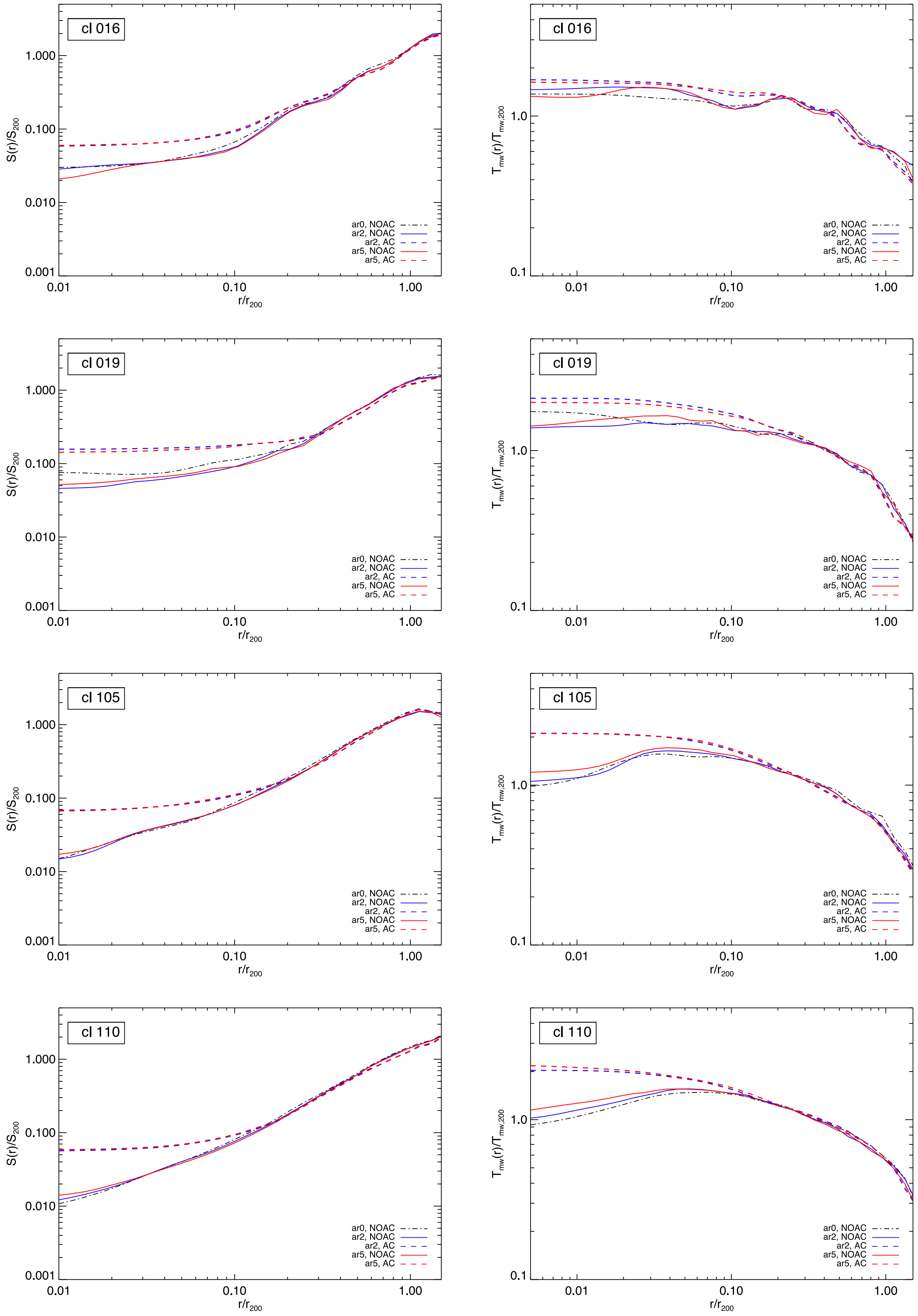

Figure 2. $z = 0$ – continued from Fig. 1.

in the figures) also show similar behaviour at small radii, where the AC profiles are noticeably higher than the NOAC ones. Different line colours in Figs 1 and 2 refer to the viscosity scheme adopted in the run, while the black, dot–dashed line always indicates to the reference simulation (ar0). From the comparison, we observe that the particular implementation of the viscosity scheme alone can already have a certain impact on the level of gas mixing, hence mildly raising the entropy of the core region (within ∼10 per cent of R_{200}), in the NOAC runs (see results by V11). However, we remark here that the introduction of the AC term seems to dominate over the numerical treatment of the viscosity, causing an increase in the central cluster entropy which is definitely more significant, in the direction indicated by the results from AMR codes.

5.1.2 Velocity power spectra

As previously investigated in V11, the implementation of a time-dependent viscosity scheme in SPH simulations of galaxy clusters can affect the characteristics of ICM motions, due to the better modelling of the AV depending on the local conditions of the shock strength. This in fact can have an additional impact on the gas mixing in cluster simulations, which is typically inhibited in standard SPH codes causing also a lower central entropy. In this work, we additionally investigate the effects of artificial conductivity on the gas motions. From the study of entropy and temperature radial profiles, we have already pointed out a significant improvement in the cluster cores due to the introduction of the AC term, which in fact favours directly the gas mixing.

In Fig. 3, we present results on the spectral properties of the gas velocity field for the adiabatic runs of the clusters in the sample. The turbulent velocity field is investigated here via the velocity power spectrum $E(k)$ (see definitions in Section 3). Each panel of Fig. 3 displays the compressive and shearing components (upper and lower insets, respectively) of the density-weighted velocity power spectrum of a given cluster. Using the same notation as for the radial profiles, the solid and dashed lines refer, respectively, to the NOAC and AC – adiabatic – simulations, while blue and red are used to distinguish between AV_2 and AV_5, respectively. The reference run (ar0; standard NOAC SPH and AV_0 viscosity) is marked by the black, dot–dashed line. In the figure, we show the velocity power spectrum components as a function of the dimensionless wavenumber $k = |\boldsymbol{k}|L_{\mathrm{sp}}/2\pi$.

From the comparison, the most striking result is that the NOAC runs show an increased spectrum amplitude for motions on the small scales (large values of k) with respect to the standard ar0 case. When the AC term is introduced, for both the viscosity schemes considered (AV_2 and AV_5), the effect is suppressed and the power spectrum is lower almost at all scales. In fact, especially for the compressive component, the AC (dashed) curves lie always below the NOAC (solid) ones.

In general, we observe that the AV scheme and the AC term have opposite, competing effects. The results obtained, valid for all the clusters analysed independently of their peculiar characteristics, suggest that while the AV scheme contributes to enhance the coherence of the velocity patterns, especially at small scales, therefore augmenting the amplitude of the power spectrum (as already observed and discussed V11), the AC term has instead the practical effect to favour gas mixing, likely contributing to more random gas motions. Overall, however, the effects due to the AC term seem to dominate and have a major impact on the properties of the gas velocity field.

5.1.3 Temperature distribution and global properties

The improvement allowed by the AC modification in the creation of cluster entropy cores has tight connections with the ICM temperature structure, as well. From the temperature profiles within R_{200} shown in Figs 1 and 2 (right-hand column), we observe that the core of the clusters tends to be hotter in the runs that include the AC term, consistently with an increase in the central entropy. This has indeed the effect of improving the gas mixing, acting as a heat diffusion term and therefore partially heating the cold gas component.

This is confirmed by the distribution of the gas temperature within the R_{200} region, shown in Fig. 4 (see also the mean temperature values reported in Appendix A). In fact, one can note a clear suppression of the fraction of gas particles with relatively low temperature ($kT \lesssim 1\,\mathrm{keV}$), with the strongest differences at $kT \lesssim 0.5\,\mathrm{keV}$. For some clusters, the amplitude of the temperature distribution is damped down by up to two orders of magnitude going from the standard NOAC runs (solid curves) to the AC ones (dashed curves). In Fig. 4, we mark the various viscosity schemes with different colours (blue and red for AV_2 and AV_5, respectively; black, dot–dashed line for AV_0). From the comparison among the different schemes, we can conclude that the impact of the AC term is dominant with respect to the effects due to the variation in the viscosity parameters. Indeed, solid lines of different colours show similar trends and the same holds, separately, for the dashed, AC curves.

From the analysis of the adiabatic runs considered here, we suggest that introducing an artificial conductivity term improves the SPH technique, which instead might produce an overabundance of cold gas in its standard formulation because of the numerical approach itself.

A qualitative impression of this effect is clearly given by the maps shown in Fig. 5, where the AC run (right-hand panel) is compared to the NOAC case, referring to both the standard and AV_2 viscosity schemes (left-hand and central panel, respectively). In the figure, we show the spatial distribution of the gas in a hot cluster (cl 011) in the sample, used as a show case. The maps all refer to the *projection* along the z-axis of the gas particles (black dots) enclosed within 1.5 times the virial radius. R_{200} is overplotted for comparison (marked as a filled circle in the NOAC cases and as a dashed circle in the AC one) and the orange points mark the cold-phase gas component ($kT < 1\,\mathrm{keV}$). From this, we observe that the large-scale structure of the cluster is preserved, with very good agreement between the runs – the cluster resides in the same position, similar in size and presenting the same major sub-structures – while the small-scale distribution of the gas is instead perceptibly different. In fact, we clearly see that especially in the cluster central regions the small, cold substructures present in the left-hand plot, and still visible in the central one, are definitely more diffused and less pronounced in the AC case (right-hand panel), where some of them are actually entirely disappeared.

Also, in order to quantify the differences related to the various viscosity schemes and to the introduction of the artificial conductivity term, we calculate for any given cluster the residuals of global intrinsic properties such as total mass and radius in the different runs, with respect to the same quantities for the cluster reference (ar0) simulation. For the region corresponding to a given overdensity Δ, we estimate such residuals as

$$\Delta Y = (Y - Y_{\mathrm{ref}})/Y_{\mathrm{ref}}, \tag{30}$$

where Y_{ref} corresponds to the same quantity calculated in the standard reference run, ar0. Results for the adiabatic simulations are shown in Fig. 6. The panels in the upper row refer to the AC runs and those in the lower row to the NOAC ones, while the different columns refer to the three typical overdensities considered: $\Delta = 200, 500, 2500$, respectively. The effects due to the different SPH modifications are expected in this case to be less significant, given the dominant role played by DM in shaping the global potential well. Indeed, this is confirmed by the residuals in mass and radius at large and intermediate radii (R_{200} and R_{500}), which are

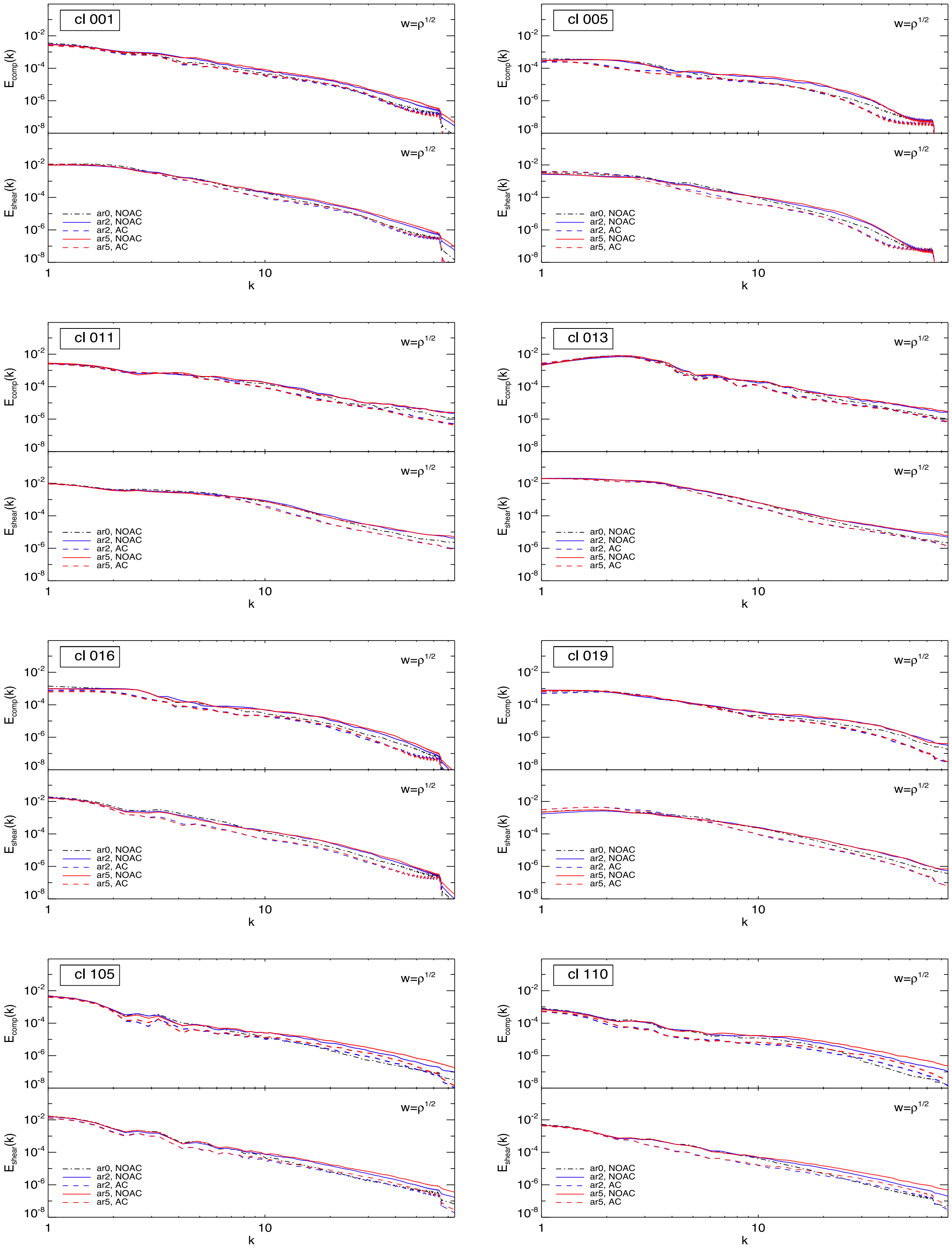

Figure 3. Velocity power spectra of the clusters in the sample, for the adiabatic simulations at $z = 0$. Line styles and colours are the same as in Figs 1 and 2.

basically consistent with zero. This indicates that, on global scale, the main characteristics of the simulated clusters do not depend on the treatment of viscosity or artificial conductivity as strongly as the thermodynamical properties of the ICM. In the innermost region (i.e. $<R_{2500}$), instead, there might be differences introduced by the AC term or the AV scheme. In the cluster core, in fact, the change of the ICM properties might play a more important role. The bias in radius, and consequently in the mass enclosed therein,

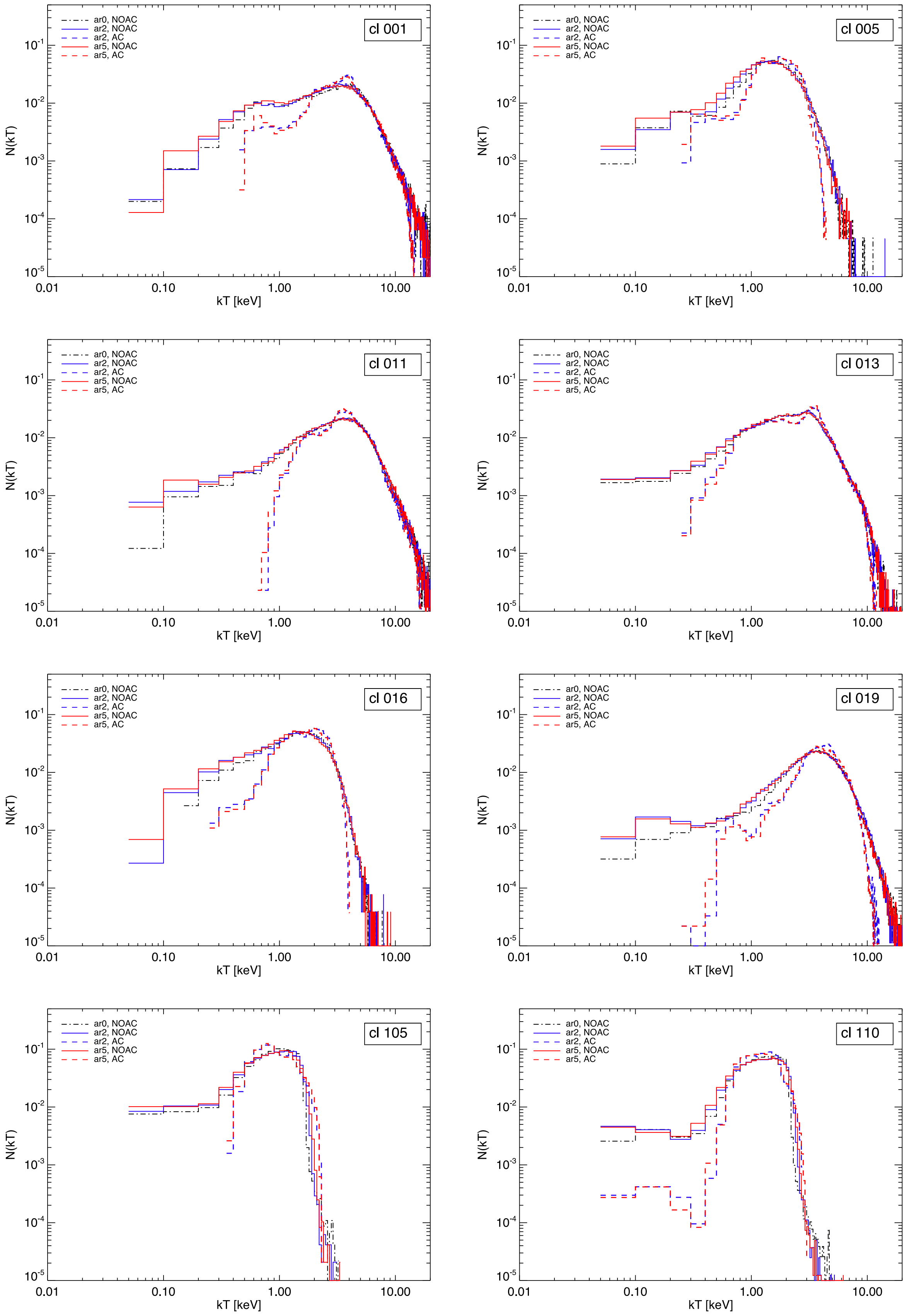

Figure 4. Gas temperature distribution within R_{200}. Comparison among the different viscosity schemes (AV$_0$: black, dot–dashed line; AV$_2$: blue; AV$_2$: red) and NOAC/AC (solid/dashed lines) runs. Adiabatic simulations at $z = 0$.

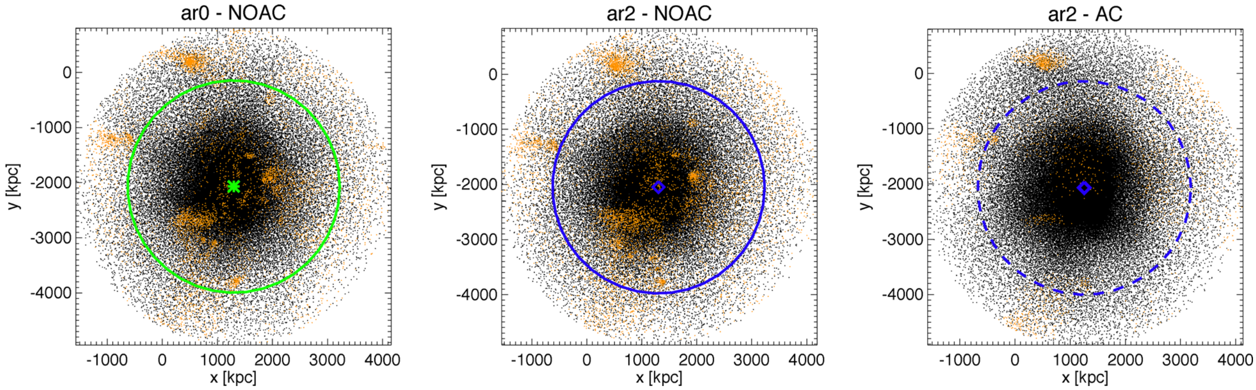

Figure 5. As an example, we show the spatial distribution of the gas particles within the R_{200}-region of cluster cl 011, at $z = 0$. The projection is made along the z-axis, for the three different runs: ar0, NOAC – ar2 and AC – ar2, respectively. Overplotted are the particles with $kT < 1$ keV (orange), the centre of the cluster and the R_{200} radius (triangle/asterisk symbols and green/blue colours are used to remark the distinction between the AV_0 – left – and AV_2 – centre and right – schemes).

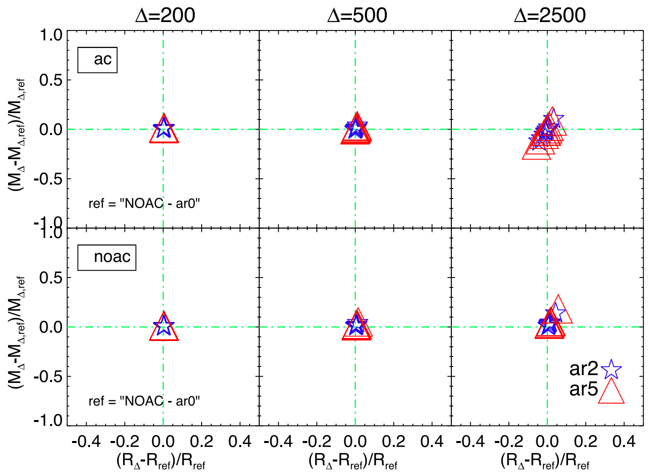

Figure 6. Differences in the global properties of the clusters for the different runs (ar2: blue stars; ar5: red triangles; AC/NOAC top/bottom panels). The variations in radius and total mass are calculated with respect to the reference run (ar0), at $z = 0$.

is different from zero by a few per cent, as seen by the last column panels in Fig. 6. We observe that in the AC runs, the majority[1] of the clusters present a smaller R_{2500} radius (and a smaller mass within it) with respect to the reference run (ar0). This trend is not as evident when only the time-dependent viscosity scheme is included in the simulations (bottom-right panel).

5.1.4 *Level of substructures: centroids and power ratios*

With centroids and power ratios, we quantify the level of substructures in the clusters of the sample, at redshift $z = 0$. Here, we still analyse the adiabatic runs (‘ar’), while deferring the discussion of radiative runs to Section 5.2.

Interestingly, the dynamical configuration of the clusters, marked by the values of w and Π_3 can be affected by the change in the numerical implementation of the SPH run, even for the same ensemble of physical processes accounted for.

This can be seen from the left-hand panel of Fig. 7, where we report the values of w and Π_3 for each cluster in the sample for standard (NOAC) and AC-SPH (upper and lower row, respectively), for various overdensities ($\Delta = 200, 500$ and 2500 in the left, central and right columns, respectively) and for the different viscosity schemes considered (different colours and symbols, i.e. black asterisks for AV_0, blue stars for AV_2 and red triangles for AV_5). In each panel of the figure, we also mark the threshold values commonly adopted to distinguish between relaxed and disturbed clusters, corresponding to $w \sim 0.007$–0.01 and $P_3/P_0 = 4 \times 10^{-8}$ (i.e. $\Pi_3 = -7.397\,94$). In the figure, we notice that especially clusters with intermediate level of substructures can undergo more relevant changes, displayed by the lines connecting the standard case (ar0; black asterisk) with the two AV_2 and AV_5 counterparts (blue stars and red triangles, respectively). Despite this, we observe a fair correlation between the two substructure estimators, basically at all overdensities, and the systems that are either significantly relaxed or strongly disturbed tend to remain so in all the runs, showing changes in the w or Π_3 that do not compromise their final classification, especially on global ($<R_{200}$) scales. At higher overdensities (i.e. $\Delta = 500, 2500$) changes among the runs can also be influenced by the changes in the thermal structure of the core, which is the region most significantly affected (as discussed in Section 5.1.1).

In Fig. 7 (right), we quantify more clearly the global changes in the cluster dynamical configuration by calculating the residuals between the w and Π_3 values in a new run with respect to the reference (ar0) case (similarly to equation 30),

$$\Delta \log_{10} w = \log_{10} w / \log_{10} w_{\rm ref} - 1 \tag{31}$$

$$\Delta \Pi_3 = \Pi_3 / \Pi_{3,\rm ref} - 1, \tag{32}$$

for the region enclosed within R_{200}.

According to equations (31) and (32), in the case of $\Delta \log_{10} w > 0$ and $\Delta \Pi_3 > 0$, the cluster would show a more relaxed configuration in the considered run with respect to the standard SPH (NOAC, AV_0) simulation. From Fig. 7 (right), we see more quantitatively that, despite some scatter, the clusters do not show any significant trend to become on average neither more relaxed nor more disturbed. Overall, we observe variations in both $\log_{10} w$ and Π_3 comprised between few and ∼10–15 per cent (generally correlated), but the distributions of the residuals are centred very close to zero, in the logarithmic scale of the figure. Typically the effect is even milder when only the viscosity scheme is modified.

---

[1] One of the clusters in the sample shows here an opposite trend, but this is the case of a very disturbed system.

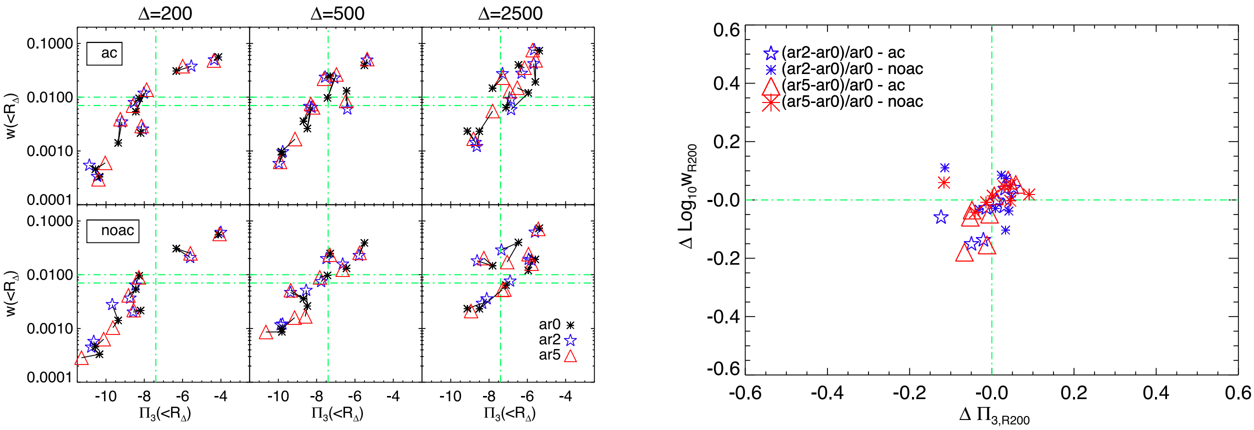

Figure 7. Left-hand panel: power ratios and centre shifts at $z = 0$, for all the various runs and overdensities as in the legend. Right-hand panel: variation with respect to the reference run 'NOAC – ar0', for $\Delta = 200$.

5.2 Radiative runs

At variance with the adiabatic runs presented in the previous sections, we consider here more realistic simulations of clusters, in which not only gravity is responsible for the structure formation, but also more complex physical processes are traced in order to describe and model the baryonic component. In this section, we discuss results for the radiative runs, where cooling of the gas, star formation, chemical enrichment and energy feedback following supernova explosions are included in the simulations. The inclusion of these physical phenomena is expected to complicate the picture discussed so far and to interact with the numerical schemes, possibly affecting the impact due to the AV and AC modifications. In order to explore this, we repeated here the same analysis done in the previous sections, using the same set of simulated clusters. In the following, we will restrict ourselves to the comparison and discussion of the most important results and, for simplicity, we will rather show them for a couple of clusters only, used as representative extreme case studies in the sample.

In this section, we will consider as reference case the radiative run: 'cr0' (NOAC, AV_0).

5.2.1 Comparison between adiabatic and radiative runs

With respect to adiabatic simulations, radial profiles of entropy and temperature for the radiative clusters seem to be less affected by either the modified viscosity scheme and the AC term, although mild differences among the various implementations can still be observed in the innermost region (<0.1–$0.2\,R_{200}$).

In Fig. 8, we display two clusters in the sample, presenting very small effects in one case (cl 011, left) and showing more significant variations of the core thermal structure in the other one (cl 019, right). The entropy and temperature profiles of the second cluster show in fact more similarities to the results discussed for the adiabatic simulations and the introduction of the AC term seems to play a more significant role in shaping the gaseous core, despite gas cooling and star formation. Overall, however, the majority of the clusters in the sample rather resemble the behaviour of cl 011, i.e. they typically do not present higher central entropy and temperature nor a significant entropy-profile flattening towards the cluster centre, with respect to standard SPH simulations.

From the velocity power spectra of the gas in the cooling runs, we can still conclude that the primary source of energy injection into the ICM consists of gravity-driven merging and accretion processes, as in fact the curves present a maximum at small wavenumbers k, corresponding to the largest spatial scales in the systems. Similarly to the adiabatic case, the major differences among the runs are still visible mainly at high values of k, corresponding to turbulent motions on small spatial scales, and are more prominent than in the adiabatic counterparts for the majority of the clusters considered.

The major difference here is that we observe a generally higher amplitude of the spectra at small spatial scales, independently of the particular run considered. For comparison, the spectrum components for the adiabatic clusters were typically spanning up to ∼six order of magnitudes (see Fig. 3), while the spectra of the radiative counterparts only span ∼two to three order of magnitudes across the k-range considered (see Fig. 9). In particular, after an initial similar decaying shape of the velocity spectrum, at $k \sim 10$ the trend is basically arrested and for $k \gtrsim 10$ both compressive and shearing components remain nearly flat or even grow again with increasing k (decreasing scale). This would suggest the presence of an additional source driving turbulence at small scales, likely linked to the development of compact cold gas clumps in the central cluster region that interact with the ambient ICM. With respect to the runs including only the AV modification (solid lines in Fig. 9), this finding is consistent with the results presented in V11.

By including the additional AC term, however, we find that this effect is moderately reduced (dashed lines in Fig. 9). Therefore, the general feature presented by the adiabatic case, where the introduction of the AC term seems to suppress the amplitude of the spectrum despite the opposite increasing trend due to the AV modification, survives the inclusion of cooling and star formation. For some clusters in the 'cr' sample (see, as an example, the case of cl 013 in Fig. 10) the impact of the AC term is even stronger than in the adiabatic case, causing the amplitude of the velocity spectrum to decrease by one to two orders of magnitude, at $k \gtrsim 50$, with respect to the runs with the AV modification only. Interestingly, this further suggests that the AC term, favouring diffusion, tends to heat the gas, smooth out the cold substructures and consequently soften the power of small-scale turbulent motions originating from the interaction between cold compact clumps and surrounding gas.

Although, on average, the effects of the AC term are not significantly visible from the radial entropy and temperature profiles, the ICM thermal structure is actually affected by it. In fact, even in the 'cr' simulations, this seems to have a systematic impact on the temperature distribution of the gas within R_{200}, reducing the fraction of the cold component with $0.1 < kT < 1\,\mathrm{keV}$. Similarly to the features discussed for the 'ar' case (Section 5.1.3, Fig. 4), the

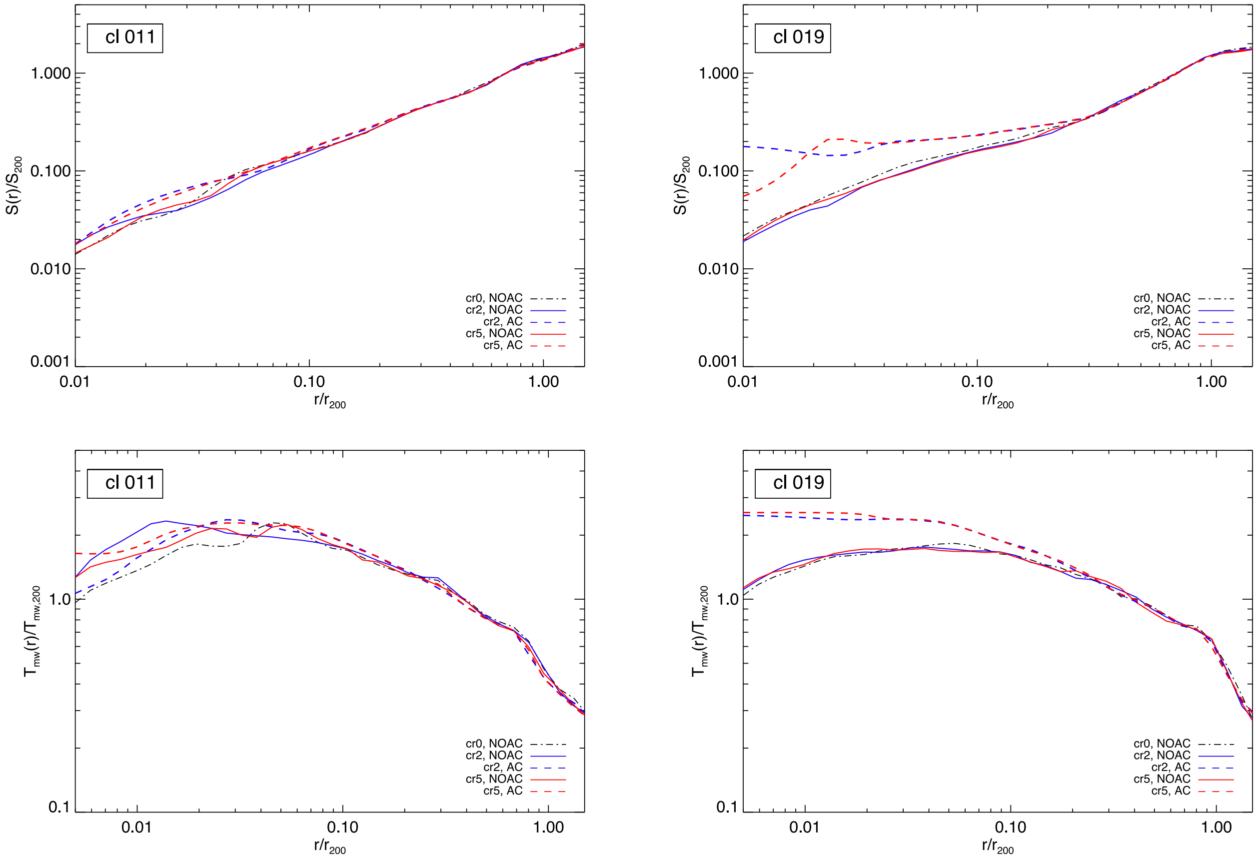

Figure 8. Similar to Fig. 1: entropy (top panels) and temperature (bottom panels) profiles for the two clusters chosen to present results from the radiative (‘cr’) runs at $z = 0$: cl 011 (left) and cl 019 (right).

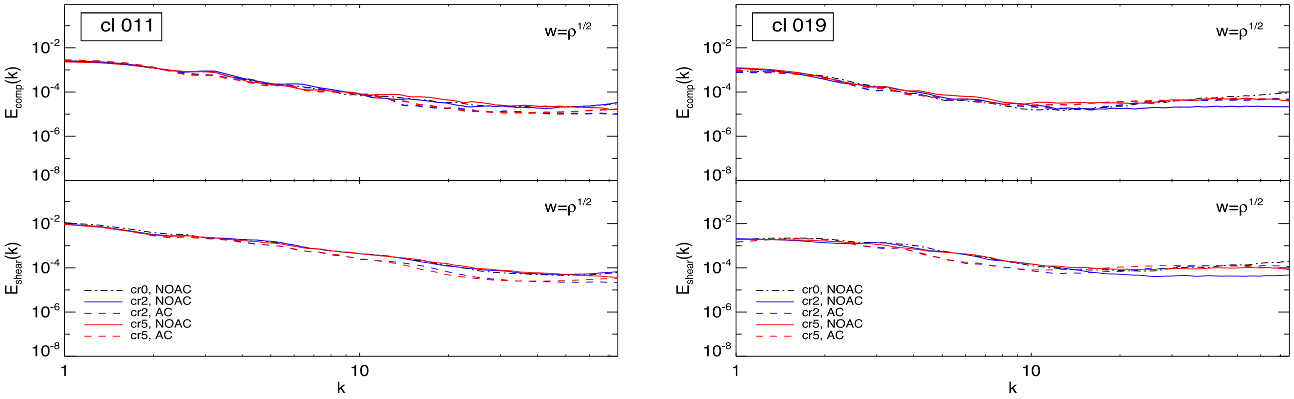

Figure 9. Similar to Fig. 3: velocity power spectra for the two clusters chosen to present results from the radiative (‘cr’) runs at $z = 0$: cl 011 (left) and cl 019 (right).

AC curves (dashed lines) in Fig. 11 show a suppression up to two orders of magnitude at low temperatures, with respect to the peak of the distribution.

The major difference in the ‘cr’ simulations is that the kT-distributions generally tend to increase again at the very low temperature end, i.e. for $kT \lesssim 0.2$–0.1 keV. We expect this very cold gas component to be associated with dense gas regions that are probably about to form stars. Nevertheless, for all the clusters of the sample the AC simulations present a significant suppression, as displayed in Fig. 11, of the cooler gas component (see also Appendix A for global mass-weighted temperatures). This confirms the robustness of the result independently of the peculiar properties of the clusters (mass, dynamics, thermal state).

Similarly to Fig. 5, we also visualize the different distribution of the cold ($kT < 1$ keV) gas in Fig. 12, for the two ‘cr’ show cases. Despite the competing effects of cooling and AC (which favours instead gas mixing and heating), we still find visible differences between the AC map (for AV$_2$; right-hand panels) and the standard NOAC ones, for both viscosity schemes (standard AV$_0$, and AV$_2$; left-hand and central panels). We confirm here the tendency to preserve the large-scale structure and the main gas substructures, while the small-scale configuration is instead clearly modified. Unlike the

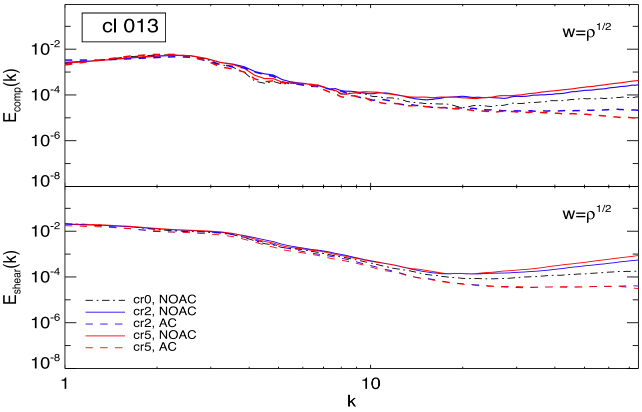

Figure 10. Velocity power spectra of a cluster (cl 013) at $z = 0$ where the effect of the AC term in suppressing the high-k tail is significant even in the 'cr' runs.

adiabatic case, however, there is here a certain persistence of the very small cold blobs even in the AC run.

In general, the results from the analysis of the 'cr' runs suggest that on the global scale, the effects due to the highly-non-linear baryonic processes are dominant with respect to the numerical treatment of both viscosity and conductivity for the gas. None the less, some noticeable effects from both of these improved SPH modifications can still be appreciated even in the presence of radiative physics.

For instance, the centroid and power-ratio diagnostics for the 'cr' clusters show that the $\mathrm{AV}_2/\mathrm{AV}_5$ and AC modifications appear to produce, on average, more regular clusters than the standard SPH-AV_0 implementation. This is displayed in Fig. 13 (left-hand panel) for the three usual overdensities and, more quantitatively, in the right-hand panel for the R_{200}-region. The residuals calculated as in equations (31) and (32) show here a mild shift towards $\Delta \log_{10} w > 0$ and $\Delta\Pi_3 > 0$, with positive variations up to ~30 per cent of both $\Delta \log_{10} w$ and $\Delta\Pi_3$. This result can still be connected to the change in the thermal properties of the gas, mainly to the heating contributed especially by the improved artificial conductivity. Interestingly, this would provide further support to the role played by turbulence in heating the ICM and therefore compensating radiative cooling (see discussion in V11 and, e.g. Fujita, Matsumoto & Wada 2004; Fujita 2005).

Other global properties, such as total mass and radius, instead, show basically no evident dependence on the particular run (see Fig. 14). Therefore, we conclude that the differences in the temperature distribution or in the dynamical indicators (both for the R_{200}-region) cannot be due to any relevant difference in the spatial selection of the gas. Only the innermost region, corresponding to an overdensity $\Delta = 2500$, presents very mild variations with respect to the reference run (cr0), similarly to what we observed for the adiabatic sample.

5.3 Observable effects on the X-ray spectra

The effects of the numerical treatment of SPH on the ICM properties can also affect the expected X-ray features, which can be highly useful for a direct comparison between simulated and observed clusters. Even though major discrepancies between numerical findings and X-ray observations are expected to relate mainly to the physical processes accounted for in the simulations, also the numerical approach itself can play a role in this.

In order to explore the effects of the AV and AC modifications of SPH on the velocity field and thermal structure of the ICM, we generate and analyse X-ray synthetic observations of the cluster core adopting the high-energy-resolution spectrometer planned to be on board the upcoming *Athena* mission (Nandra et al. 2013). The motivation for this choice resides in the possibility to reliably constrain the gas (l.o.s.) velocity dispersion from the detailed spectral analysis of well-resolved emission lines from heavy ions (e.g. iron), for which the line broadening can be dominated by non-thermal motions rather than by thermal ones (see e.g. Inogamov & Sunyaev 2003; Sunyaev, Norman & Bryan 2003; Rebusco et al. 2008). Such studies, in fact, require very good energy resolution of the X-ray spectra, unreached so far with current telescopes but definitely achievable by next-generation instruments, like the *Athena* spectrometer.

For the present study, *Athena*-like spectra were obtained by means of the X-ray photon simulator PHOX[2] (for details on the code, we refer the reader to Biffi et al. 2012; Biffi, Dolag & Böhringer 2013b).

As a first step, we focus on the adiabatic sample, for which the possible degeneracies due to radiative physics, that might compromise the X-ray appearance of the clusters, are avoided. As such, the pure effects due to the numerical modifications of SPH can be more clearly singled out. In particular, we considered the adiabatic simulations for a single viscosity scheme (namely, the ar2 runs) and generated the synthetic spectra for both the standard NOAC clusters and for their AC counterparts. Here, we consider the simulation outputs at $z \sim 0.05$.[3] An average metallicity of $0.3\,\mathrm{Z}_\odot$ was assumed for all the SPH gas particles in the simulations, with the solar abundances assigned following Anders & Grevesse (1989). The X-ray synthetic photons were generated from each gas element assuming a typical absorbed APEC model (Smith et al. 2001) for a collisionally-ionized plasma. The equivalent hydrogen column density parameter for the WABS model (Morrison & McCammon 1983) was fixed to the value of $10^{20}\,\mathrm{cm}^{-2}$. The final X-ray spectra were obtained by assuming a fiducial exposure time of 50 ks and the response matrix file of the *Athena* X-IFU instrument.[4]

In order to evaluate the observable impact on the X-ray spectrum due to the changes in the ICM thermal structure and velocity field due for different numerical implementations, we want to focus on the central region of the clusters. For the given cosmological parameters and the very low redshift considered here, however, the field of view of the X-IFU spectrometer is relatively small (5 arcmin × 5 arcmin) and only covers a region with ~300 kpc diameter (physical units). Therefore, despite convolving the ideal photon list generated with PHOX with the response of the chosen instrument, we assume to cover instead a larger cluster-centred projected region, enclosed within a radius of ~300 kpc – corresponding to ~15–34 per cent of R_{200}, for the selected clusters. Observationally, this would require a multiple-pointing observation of the clusters with the X-IFU instrument.

In Fig. 15, we display a case example in order to compare the mock spectra for the NOAC (black, solid) and AC (red, dotted) ar2 runs of the same cluster. Qualitatively, one can already appreciate the main difference between the two data sets, namely the lower

---

[2] See http://www.mpa-garching.mpg.de/~kdolag/Phox/.

[3] The redshift adopted in this analysis is not exactly equal, albeit very close, to $z = 0$ in order to avoid the divergence of the luminosity distance and allow for realistic calculations of the X-ray emission.

[4] Available on the *Athena* mission website http://www.the-athena-x-ray-observatory.eu/.

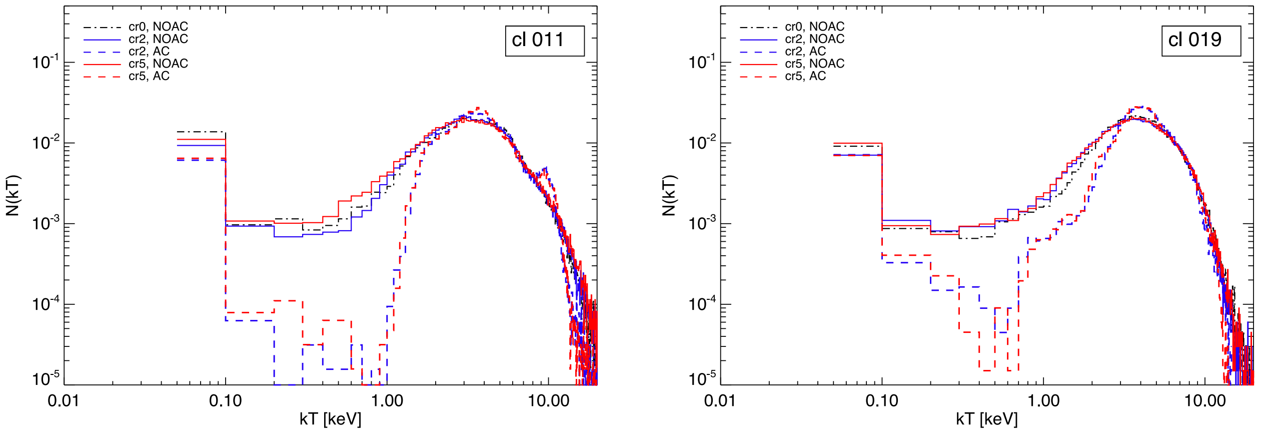

Figure 11. Similar to Fig. 4: gas temperature distribution within R_{200} for the two clusters chosen to present results from the radiative ('cr') runs at $z = 0$: cl 011 (left) and cl 019 (right).

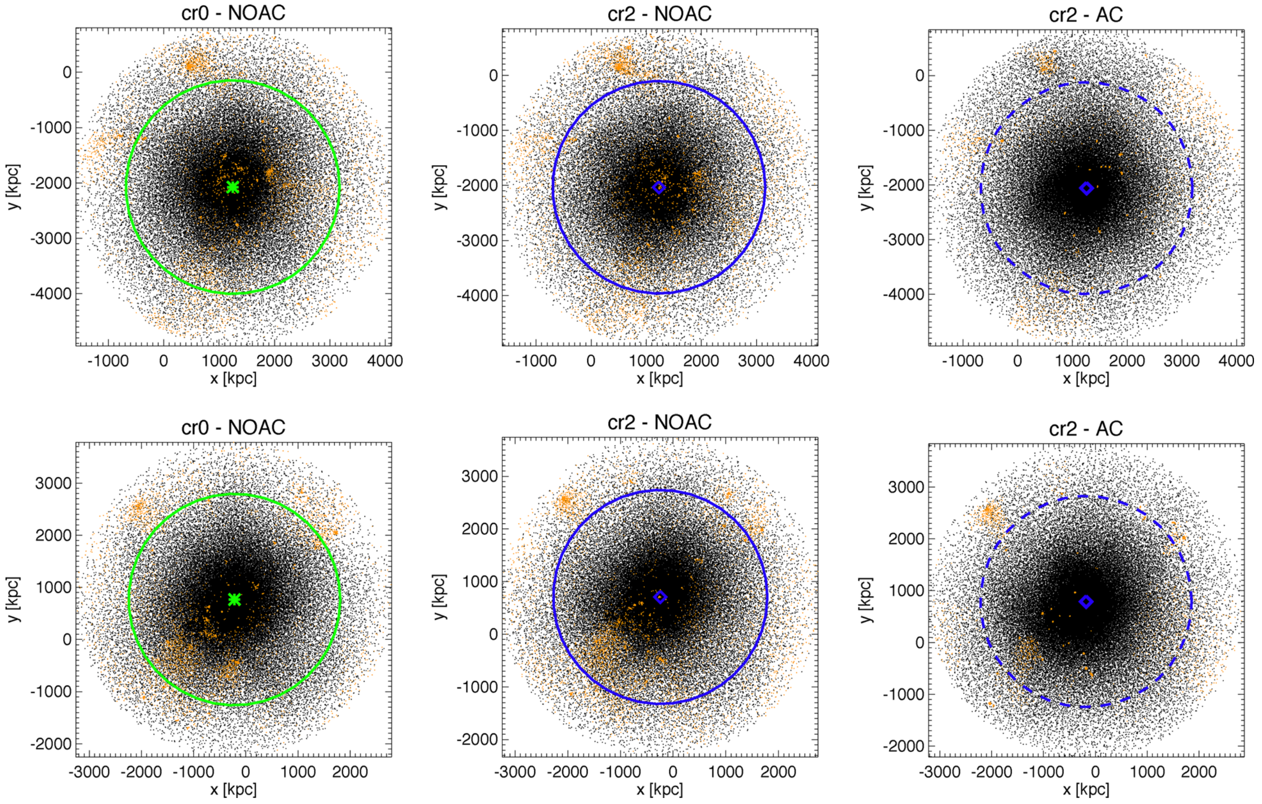

Figure 12. Same as Fig. 5, but for the two example cases chosen to present radiative ('cr') runs, at $z = 0$: cl 011 (top) and cl 019 (bottom).

normalization of the AC spectrum. For a better visualization, we choose the case of a massive system (cl 019) where the difference between the runs is particularly evident. This is the likely consequence of the reduced amount of cold gas in the AC runs, already discussed in Sections 5.1.1 and 5.1.3 (see Figs 1 and 2 for the differences in the cluster central region from the temperature profiles and, for global scales, Fig. 4), as the suppression of cold and dense X-ray-emitting gas eventually causes the number of photons to be smaller in the AC spectra. More quantitatively, always referring to the ar2 runs, the original generation of photons from the simulation output provides for the NOAC clusters, on average, a factor of ∼2 more photons than for their AC counterparts. By applying the projection unit of PHOX and restricting the selection to the (projected) virial radius, this ratio is still roughly preserved across the sample. Finally, when also the convolution with the instrumental response is taken into account and only the central region is selected to generate the synthetic spectra, the suppression of observed photons in the AC runs is conserved for the smaller systems and it is even stronger for the hotter clusters, for which we obtain spectra with a total number of counts smaller by a factor up to 2.5–3 with respect to the NOAC case.

We expect these observable differences to depend only on the details of the ICM thermal structure and velocity field, mainly determined by the inclusion or omission of the AC term. In fact, for any given cluster: (i) we consider a single viscosity scheme; (ii) we consider the same spatial selection for the mock observation, and

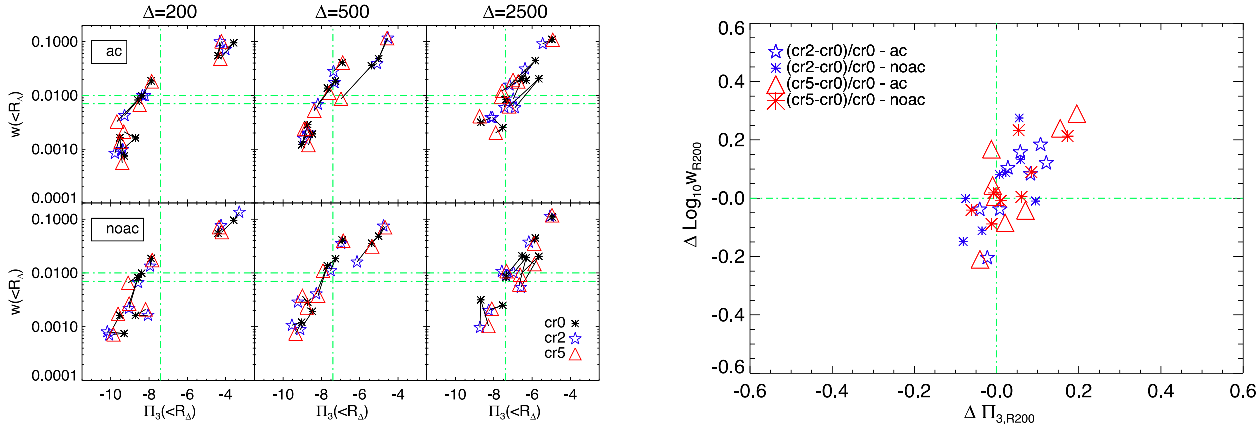

Figure 13. Same as Fig. 7, but done for ‘cr’ runs.

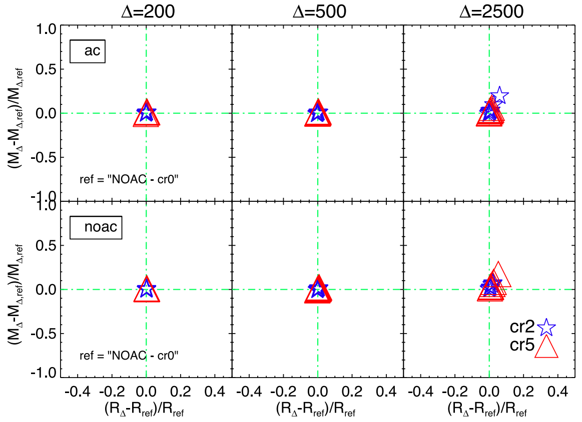

Figure 14. Same as Fig. 6, but done for ‘cr’ runs.

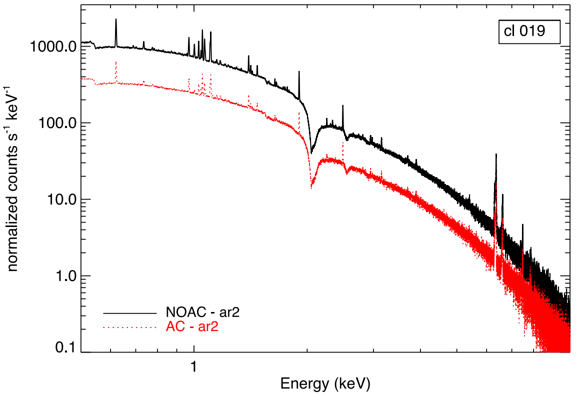

Figure 15. *Athena* X-IFU high-resolution spectrum of a massive cluster (cl 019) in the sample simulated with the standard SPH code (NOAC – black, solid line) and with the AC term (red, dotted line). Here, as a test case, we only compare the two adiabatic runs (ar2) for the same viscosity scheme (AV_2). The projected region considered is that enclosed within 300 kpc from the cluster centre.

for the same viscosity parameters the sizes of the NOAC cluster and its AC counterpart are not dramatically different; and (iii) we generate the ideal emission assuming fixed values for gas metallicity, redshift and Galactic absorption, reducing therefore the possible additional degeneracies. Overall, this can have an impact on the global luminosity. Despite these mock observations are not best suited for such a study, we can expect also the global X-ray luminosity of the adiabatic clusters to be partially reduced by the changes in the ICM thermal structure due to the AC term. In other words, this would suggest that the tendency of adiabatic simulations to produce ‘overluminous’ clusters (see, e.g. discussions in Biffi et al. 2014; Planelles et al. 2014) cannot be entirely ascribed to the role played by the physical processes not accounted for, as also the standard SPH method itself can have an impact on the results.

5.3.1 *Velocity broadening of spectral lines*

Moreover, the spectral analysis of the restricted 6–7 keV band (comprising the Fe lines at 6.4 and 6.7 keV) specifically allowed us to derive estimates for the average l.o.s. velocity dispersion of the gas across the central projected 600 kpc. To do this, we made use of the publicly available XSPEC package (v.12.7.1; see Arnaud 1996) and fitted the spectra with an absorbed, velocity-broadened APEC model (BAPEC model), which assumes the distribution of the gas non-thermal velocity along the l.o.s. to be Gaussian and the broadening is quantified by the standard deviation, σ, of the distribution. In the fit, normalization, temperature, σ and redshift were free to vary. From the variation in redshift, known precisely from the simulation output, one can ultimately evaluate the mean l.o.s. bulk motion of the gas as an energy shift in the centre of the iron emission line.

We remark here that the motions detectable in this way, however, are those along the l.o.s. through the cluster, so that they also include the contribution from global motions on the large scale (e.g. due to streaming patterns, rotation, etc.), in addition to the small-scale turbulence. None the less, even though the whole cluster size along the l.o.s. contributes to the emission, we expect a relatively low contamination from the foreground and background gas residing in the cluster outskirts. In fact, by considering the Fe emission line, we mainly focus on the motions of the hot-gas component, which resides principally in the central cluster region, especially for the low- and intermediate-mass systems.

As an example, we show in Fig. 16, the case of the hot system cl 019, where the Fe complex lines at ~6.4 and ~6.7 keV (rest-frame-energies) are very well visible in the X-ray spectrum. Comparing the NOAC (black, solid line) and AC (red, dotted line) spectra, we observe immediately the aforementioned different normalization. Furthermore, we can also appreciate qualitatively the different shape and broadening of the lines, especially for the 6.7 keV one (inset panel). In fact, the red, dotted (AC) line profile presents more sharp features, while the broadening of the black profile is clearly more significant. This difference in the line broadening is

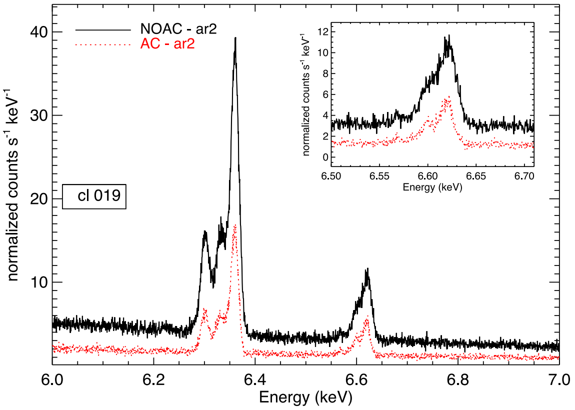

Figure 16. Visualization of the Fe complex at 6.4 keV and zoom on the 6.7 keV line for a hot system (cl 019). The standard NOAC (black, solid line) and AC (red, dotted line) runs are compared, for the same AV$_2$ viscosity scheme.

quantitatively estimated in the spectral fit via the σ value, which differ by about ∼50 km s^{-1}:

$$\sigma^{\rm NOAC}(\mathrm{cl019}) = (349.710 \pm 2.244\,64)\,\mathrm{km\,s^{-1}}$$
$$\sigma^{\rm AC}(\mathrm{cl019}) = (297.460 \pm 3.055\,33)\,\mathrm{km\,s^{-1}}.$$

Remarkably, given the very good spectral resolution of the *Athena* spectrometer at the energies of interest (∼few eV), the difference between the σ values for the two different cluster simulations considered (NOAC and AC, both for AV$_2$) can be distinguished down to few tens of kilometres per second. Such result, however, could not be easily tested for the colder systems in the sample, where the Fe lines in the mock X-ray spectra are not very bright features and a reliable fit cannot therefore be pursued.

In general, the result of this exercise suggests very promising prospects about the performance of the next-generation high-resolution X-ray instruments (like *Athena*, but also *ASTRO-H*) in the study of cluster gas motions. Here, however, we note that this test was performed with idealized conditions, mainly due to the use of adiabatic simulations, fixed average metallicity – which would otherwise represent an additional free parameter in the fit – and no inclusion of an X-ray background. The purpose of the present analysis, in fact, solely concerns the effects of the proposed numerical modifications on to the X-ray observable properties of simulated clusters, which can be very sensitive to the gas thermodynamical structure and are none the less crucial in order to properly compare simulations and observations.

5.3.2 Comparison with radiative cluster simulations

Similarly to the results presented in the previous sections, also the X-ray synthetic properties of the radiative cluster simulations are evaluated, and the comparison with the adiabatic case can be discussed. Synthetic X-ray data have been generated with PHOX, by adopting exactly the same set of observational parameters and instrumental responses used for the adiabatic clusters, except for the physical properties of the systems, such as the centre of the gas distribution on which the pointing is centred.

Despite the possibility to account for the specific metallicity of the gas elements followed within the radiative simulations, we decide to artificially impose a fixed metallicity here, 0.3 Z$_\odot$, like for the adiabatic clusters. The motivation for this choice is that we intend to study and single out especially the effects of the numerical SPH implementation – of the AC term, in particular – reducing as much as possible any additional source of degeneracy. Here, we limit the discussion to the interplay between the AC term and the baryonic physics (gas cooling and star formation). In fact, a metallicity value or metal abundances that vary for each gas element would further increase the level of complexity of the spectrum, affecting the comparison of different clusters and between radiative and adiabatic runs.

We find that the results from the synthetic X-ray observations of the cooling-run clusters basically mirror the effects discussed in Section 5.2. The major differences introduced by the AC term are substantially smoothed out, with respect to the adiabatic case, by the account for baryonic physical processes that dominate in shaping the cluster final thermodynamical properties. The core region observed here shows in fact that the impact of the numerical scheme (mainly the AC term) can vary from cluster to cluster, overall presenting no systematic formation of an entropy core, except for few exceptions (see, e.g. Fig. 8). Similarly, the suppression of the intermediate–low temperature gas can influence differently the final X-ray spectrum depending on the particular cluster considered. Essentially, while such cold-gas suppression appears to be a common characteristics also for all the clusters in the radiative set (Section 5.2), the importance of this effect in the core can vary from case to case. We remind, in fact, that the innermost cluster region is more significantly affected by cooling and star formation processes, to which the very cold gas ($kT < 0.1$ keV) is still associated in spite of the partial mixing and heating driven by the AC term.

More quantitatively, we find that the NOAC clusters still tend to typically produce more (on average by 30 per cent) photons than the AC counterparts. The precise factor, however, varies significantly across the sample, ranging from ∼1.1 up to ∼2.3, with a single case where the amount of photons in the NOAC case is even less than in the AC one. This remarks how important are the specific ICM properties, mainly determined by the baryonic physics.

Following Section 5.2, we propose the same examples to represent two opposite behaviours: the clusters in Fig. 17 show, in fact, very similar NOAC/AC mock spectra in one case (cl 011, left) and very different ones in the other (cl 019, right). Fig. 17 also shows the zoom on to the 6–7 keV energy band, comprising the iron emission lines targeted to measure the amplitude of l.o.s. gas motions. Concerning this diagnostics, we already discussed for the adiabatic case the impossibility to draw a common conclusion for all the clusters in the sample, given the importance of their particular characteristics. When the cooling runs are concerned, this caveat is still valid. Nevertheless, for the most prominent iron lines visible in some of the cluster spectra, we still generally observe a sharper line profile in the AC case and a more broadened shape in the NOAC ones (red-dotted and black-solid lines, respectively; lower-row panels). Again, this can be related in some degree to the enhanced gas mixing and heating in AC clusters, which reduces the amount of cold dense clumps and, in turn, the turbulence driven by the hydrodynamical instabilities originating from their interaction with the ambient ICM.

6 DISCUSSION

The generation of mock X-ray observations of the simulated clusters has further confirmed the effective impact of the particular implementation of SPH on the physical properties of the ICM and, consequently, on their observable features.

The main result of the different gas thermal distribution, found when the AC term is included, is that the amount of X-ray photons

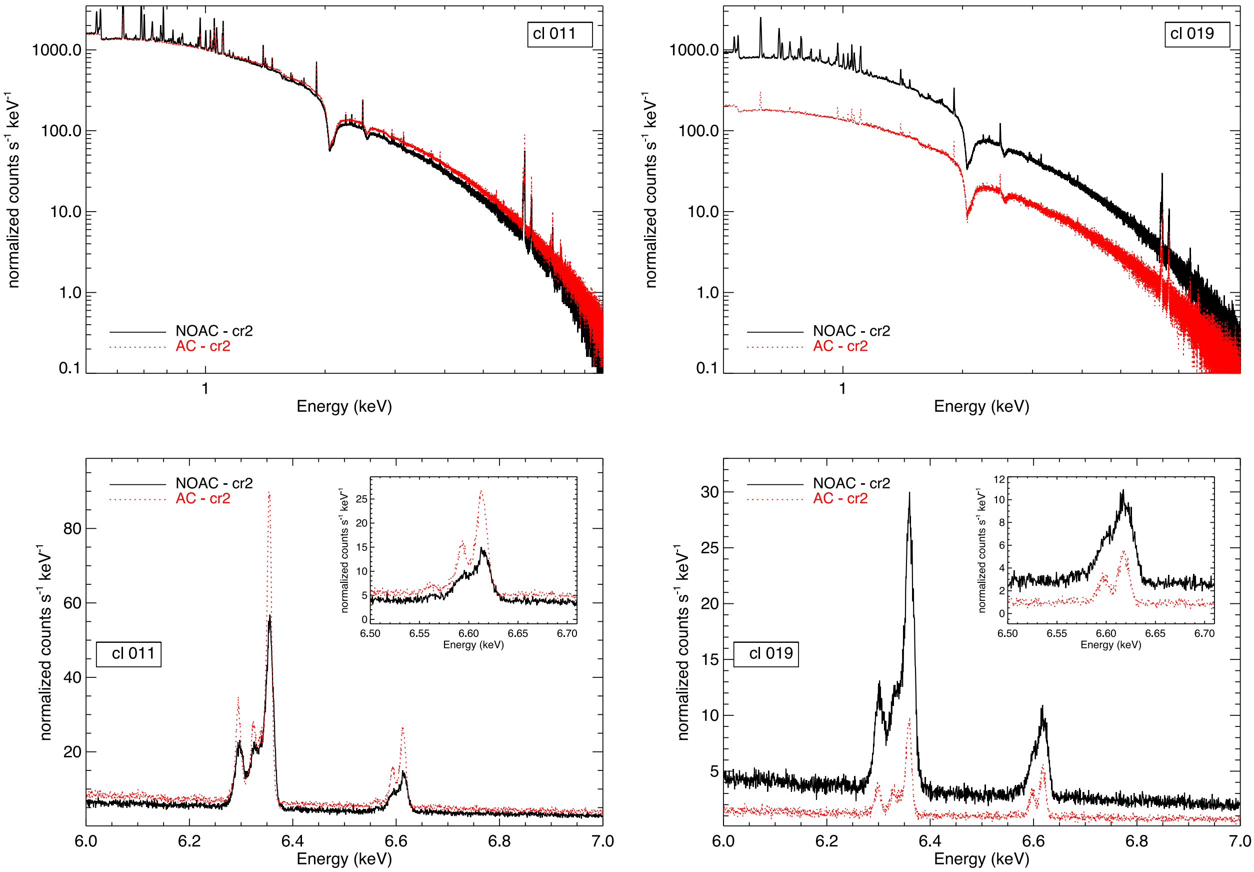

Figure 17. Same as Figs 15 and 16, but for the two example clusters used to show results from the radiative ('cr') runs: cl 011 (left) and cl 019 (right).

produced from the adiabatic clusters is significantly reduced with respect to the standard-SPH runs. This is the consequence of the suppression of the cold dense gas component, which is responsible especially for the soft-X-ray emission. This effect is visible already before taking into account the projection and instrumental response, but survives after these.

In the cooling runs, X-ray synthetic spectra confirm that the radiative physics does play a major role, softening the differences induced by the numerical treatment of SPH. Nevertheless, a general decrease of the total amount of X-ray photons produced for the AC clusters is still present, although less systematic. Focusing the analysis on the cluster core, moreover, contributes to reducing the differences between AC and standard SPH runs, since the central part of the cluster is particularly affected by baryonic processes such as cooling, star formation and feedback, likely to happen on shorter time-scales than the diffusion favoured by the artificial conductivity.

The instrument adopted to derive mock X-ray observations, the high-resolution spectrometer (X-IFU) designed for the upcoming *Athena* mission, is chosen here for testing the possibility to constrain ICM bulk and turbulent velocities from well-resolved bright emission lines in X-ray spectra (see also Biffi, Dolag & Böhringer 2013a; Biffi et al. 2013b). From the spectral analysis of the Iron lines in the 6–7 keV band, we find velocity differences from cluster to cluster and between AC and NOAC runs down to few tens of $\mathrm{km\,s^{-1}}$. With the high spectral resolution achievable with next generation of X-ray instruments such as *ASTRO-H* and *Athena*, observational studies of this sort will become possible and motions in the ICM will be measured with unprecedented level of detail (Bianconi, Ettori & Nipoti 2013; Biffi et al. 2013b; Nagai et al. 2013; Gaspari et al. 2014). Combining this with high spatial resolution (e.g. with *Athena*), the ultimate goal will be to spatially constrain the plasma velocity field (Ettori et al. 2013).

Even though turbulent and bulk motions cannot be easily disentangled, progresses in this direction are needed in order to observationally constrain ICM turbulence models, bracket the possible sources of deviation from hydrostatic equilibrium and, for instance, better understand the bias in the X-ray mass reconstructions, likely affected by non-thermal pressure contributions and temperature inhomogeneities (e.g. Fang, Humphrey & Buote 2009; Lau, Kravtsov & Nagai 2009; Biffi, Dolag & Böhringer 2011; Rasia et al. 2014).

These observational uncertainties on the amount of turbulence present in the ICM pose the issue to ascertain whether the numerical resolution employed in our simulations is adequate to capture the main features of ICM turbulent motion. In the absence of direct measurements of turbulent velocities, indirect constraints on the magnitude of ICM viscosity can be extracted by measuring some ICM properties.

One possible method is to investigate the structure of cold fronts (CFs; Markevitch & Vikhlinin 2007) in the sloshing scenario (ZuHone, Markevitch & Johnson 2010; Roediger et al. 2011, 2013a, 2013b), since the growth of KHI is suppressed in presence of sufficient ICM viscosity. Along this line of reasoning, Roediger et al. (2013a) investigated the structure of sloshing CFs in the Virgo cluster, using surface brightness profiles from *XMM–Newton* data, showing that for a Spitzer-like viscosity a suppression factor $f_{\mathrm{V}} \sim 0.1$ is needed to avoid suppression of KHI at CFs. The corresponding Reynolds number $\mathrm{Re} = UL/\nu$ can be written as (Roediger et al. 2013a)

$$\mathrm{Re} \sim \frac{140}{f_{\mathrm{V}}}\left(\frac{U}{300\ \mathrm{km\,s^{-1}}}\right)\left(\frac{L}{100\,\mathrm{kpc}}\right)\left(\frac{\rho_{\mathrm{g}}}{10^3\rho_{\mathrm{c}}}\right)\left(\frac{T}{3\,\mathrm{keV}}\right)^{-5/2}, \tag{33}$$

where L is the characteristic injection scale, U is the characteristic velocity, ρ_{g} the gas density and $\nu \propto T^{5/2}n^{-1}$ is the kinematic viscosity of the medium.

Another indirect approach to probe the presence of turbulence in the ICM is to analyse the power spectrum of gas density fluctuations (Schuecker et al. 2004; Gaspari & Churazov 2013; Gaspari et al. 2014). In a recent paper, Gaspari & Churazov (2013) studied the effects of thermal conduction and turbulence in the ICM using high-resolution hydrodynamical simulations of the Coma cluster. By comparing the gas density fluctuation spectrum of the simulations against deep *Chandra* observations, they were able to put strong upper limits on the thermal conduction suppression factor f_{C}. The best accord is obtained for simulations with $f_{\mathrm{C}} \lesssim 10^{-3}$ and mild subsonic turbulence with Mach number $M \sim 0.45$. For these simulations the Reynolds number is $\mathrm{Re} \lesssim 500$.

The Reynolds number $\mathrm{Re}_{\mathrm{sim}}$ for our SPH simulations can be derived by equating the AV terms to a corresponding physical Navier–Stokes viscosity (Price 2012a,b), so to obtain

$$\nu_{\mathrm{SPH}} \sim \frac{1}{10}\alpha v^{\mathrm{AV}} h. \tag{34}$$

To estimate $\mathrm{Re}_{\mathrm{sim}}$, we set α to the floor value $\alpha_{\mathrm{min}} \sim 0.01$ of the AV_5 run, v^{AV} to the sound velocity from equation (7) and h is computed using equation (2). We then obtain

$$\mathrm{Re}_{\mathrm{sim}} \sim 3500\left(\frac{M}{0.3}\right)\left(\frac{0.01}{\alpha}\right)\left(\frac{L}{100\,\mathrm{kpc}}\right)\left(\frac{\rho_{\mathrm{g}}}{10^3\rho_{\mathrm{c}}}\frac{10^8\,\mathrm{M}_{\odot}}{m_{\mathrm{g}}}\right)^{1/3}. \tag{35}$$

A comparison between equations (33) and (35) shows that the two Reynolds numbers are of comparable size. Note however that setting α_{min} to 0.1, as in the AV_2 run, would have reduced $\mathrm{Re}_{\mathrm{sim}}$ by an order of magnitude, whilst the simulation results indicate little variations between the AV_2 and AV_5 runs.

We therefore, conclude that our findings are not affected in a significant way by the numerical resolution of the simulations.

In particular, despite the success of our AC implementation in alleviating the problem of standard SPH in treating the gas mixing, our results from radiative runs suggest that the effects seen in adiabatic clusters are less pronounced when gas cooling and star formation are accounted for. Radiative physics basically dominates the resulting ICM properties, mainly acting on time-scales smaller than those set by diffusion. Moreover, the possibility to rely on physical conduction to overcome the cooling-flow problem seems very unlikely (see, e.g. Dolag et al. 2004; Gaspari & Churazov 2013) and we do not expect a very significant impact due to physical thermal conductivity in real clusters.

On the numerical simulation side, the effort to investigate and predict the observable signatures of the ICM thermal and dynamical state carried by its X-ray emission is crucial for a faithful comparison to observational findings.

None the less, from the present analysis, it turns out that the numerical implementation itself of the SPH method can impact the ICM state in a way that is not negligible, as in fact the effects can be still appreciated from the final X-ray mock observations. Namely, they must be profound enough to survive the complication due to 2D projection and convolution with instrumental effects. Standard SPH, in particular, seems to overpredict per se the X-ray emission from the ICM and this can be visibly alleviated by introducing a heat-diffusion term (AC), which contributes to smooth out small-scale substructures of cold dense gas. By increasing the entropy mixing and heating the colder gas substructures, such diffusion term basically suppresses the sources of hydrodynamical instabilities, mainly generated by cold clumps moving in the ambient ICM. The resulting damping of small-scale motion amplitude, found to be a systematic result for all our clusters in AC-SPH (both adiabatic and radiative) runs, is also mirrored by the different broadening of the Fe emission lines, which typically present sharper features than for standard SPH simulations.

Overall, the combined implementation of the time-dependent AV and artificial conductivity schemes points in the direction of bridging the gap between SPH and Eulerian codes, by partially alleviating the commonly known problems of the Lagrangian approach in resolving the turbulent field and, simultaneously, reducing the amount of overabundant, cold gas clumps.

7 CONCLUSIONS

In this paper, we have presented results extracted from a suite of hydrodynamical simulations of galaxy clusters. The ensemble has been constructed from various runs with different hydrodynamical parameters, starting from the same set of initial conditions. The code we use is an improved SPH scheme which employs a time-dependent AV parameter and an artificial thermal-diffusion term (AC). The latter has been introduced with the purpose of resolving the lack of entropy mixing which in standard SPH inhibits the growth of instabilities. These improvements in the SPH method are motivated by the difficulty in achieving consistent results between hydrodynamical simulations produced by AMR and SPH codes, an issue on which recently there has been a significant debate by many authors, as already outlined in Section 1.

Our study is aimed at assessing the impact on ICM properties of the simulated clusters due to the new AC-SPH scheme. In the following, we summarize our main results.

(i) Introducing the AC term has a significant impact of the thermodynamical properties of the ICM, in particular the cores of the simulated clusters exhibit higher entropies and temperatures than in the standard scheme. This is a consequence of the gas mixing driven by the new diffusion term.

(ii) In particular, for the adiabatic runs, the level of core entropies is now consistent with those predicted by AMR codes, pointing towards numerical convergence between the two approaches.

(iii) The temperature structure of the ICM is significantly altered in simulations that incorporate the AC term, with central temperatures higher than in the standard runs. We find that the cooler part ($T \lesssim$ 1–0.5 keV) of the temperature distribution is strongly suppressed.

(iv) The time-dependent AV scheme is effective in reducing viscous damping of velocities associated with AV and spectral analysis shows at high wavenumbers velocity power spectra amplitudes which are higher than in the no-AV case. However, this effect is significantly reduced when the AC term is introduced. This follows because the gas mixing induced by the diffusion term favours the evaporation of cold dense substructures, which are responsible for the instabilities originating at the surface between the moving clumps and the ambient ICM and in turn for the generation of turbulence.

(v) The morphological estimators we use to quantify the level of substructures do not show significant changes among different runs. This is consistent with the finding (see Figs 5 and 12) that the presence of the AC term modifies the small-scale thermal structure of the gas, while leaving unaffected the scales probed by our estimators ($\gtrsim R_{2500}$).

(vi) For the cooling runs, these findings are still present, although not with the strength exhibited by adiabatic simulations. In particular, the suppression of the cooler part of the temperature distribution is less pronounced and very cold blobs survive in the inner parts of the clusters. This is clearly indicative that the time-scales set by the diffusion term are much larger than the ones set by the cooling rate.

About the first item, it is worth noting that the convergence between the final levels of core entropies produced in grid-based cluster simulations and the ones obtained with the AC-SPH code used here is strongly indicative of the effectiveness of the adopted numerical scheme in solving some of the inconsistencies present in standard SPH. However, this still leaves open the issue of determining the *correct* level of central entropy which is produced in non-radiative simulations of galaxy clusters. In Eulerian mesh codes, there is a fluid mixing which occurs at the cell level and is inherent to the method itself. Therefore, a certain level of overmixing is present in AMR simulations (Springel 2010b). This suggests that the correct results lies between the range bracketed by standard SPH and AMR. To overcome the difficulties present in both SPH and AMR methods, (Springel 2010b) proposed a new scheme in which the hydrodynamical equations are solved on a moving unstructured mesh using a Godunov method with an exact Riemann solver (AREPO). The new code has been tested in a variety of test cases (Sijacki et al. 2012). To further investigate this issue, it would be interesting to directly compare ICM entropy profiles from non-radiative cluster simulations obtained with such different numerical codes.

The above findings are also consistent with the results presented in a recent paper by Rasia et al. (2014), in which the authors investigate the differences in thermal structure of the ICM in cluster sets simulated using either the standard SPH or the AMR method. In particular, non-radiative simulations performed with the AMR code show in the cluster inner regions variations in temperature much smaller than in the SPH runs. This is due to the absence in standard SPH of gas stripping of cold blobs and substructure evaporation owing to its limitations in handling fluid instabilities, whilst the AC-SPH scheme has been proved to be successful in passing the blob test (see section 3.4 of Valdarnini 2012). However, these differences are strongly reduced when radiative losses are taken into account, since cold dense gas is more quickly removed.

In summary, the most important aspects of our results is that in hydrodynamical simulations of galaxy clusters, incorporating the AC term within SPH has a direct influence on the global thermal structure of the ICM, and not only in cluster cores. The changes are significant in adiabatic simulations and still present, though with a lesser extent, in cooling runs. We expect these improvements in the physical modelling of the ICM to be rich of implications in many aspects which exploit results of hydrodynamical simulations of galaxy clusters as tools to test cosmological models.

First, introducing the AC-SPH scheme to perform the simulations is likely to have a significant impact on the so-called overcooling problem (Borgani & Kravtsov 2011), in which the fraction of cooled gas which is turned into stars is higher than observed. The new term is expected to strongly reduce the survival of cold blobs in cluster inner regions because gas stripping is much more efficient, thereby reducing the amount of cold dense gas available to form stars.

Secondly, the amplitude of the thermal Sunyaev–Zel'dovich (tSZ) power spectrum depends on the electron pressure profile. This will be affected by the modifications in entropy and temperature of the ICM expected in cluster simulations performed using the AC-SPH code. It is not straightforward to predict the impact of these changes on the final tSZ spectrum since the spectrum itself is redshift- as well as scale-dependent. None the less, the changes should go in the direction of a lower spectral amplitude, since the rise in temperature is accompanied by a decrease in central density and in turn by a lower hot-gas pressure profile at the cluster centre. These modifications in the predictions of the tSZ power spectrum amplitude might eventually reduce the tension between the best-fitting values of cosmological parameters, such as σ_8 and $\Omega_{\rm m}$, extracted from current measurements (McCarthy et al. 2014).

Lastly, the modifications in the thermal structure of the ICM will also affect the bias of the X-ray mass estimator based on hydrostatic equilibrium. Rasia et al. (2014) find that at $\sim R_{500}$ the mass bias in standard SPH simulations can be a factor ∼2 larger than in the corresponding AMR runs. We expect these differences to be reduced in the new AC-SPH scheme. We plan to investigate these issues in a more systematic way in a forthcoming paper in which we will use the new numerical scheme to construct a large set of hydrodynamical simulations of galaxy clusters, designed to cover more than a decade in cluster masses.

Efforts to study the role of numerics in shaping the final appearance of simulated galaxy clusters are definitely necessary in order to fully single out the effects purely due to the baryonic physics and finally constrain its modelling, which is essential to match and interpret observations of real clusters.

ACKNOWLEDGEMENTS

The authors acknowledge the anonymous referee for helpful comments that contributed to improve the presentation of our results and the quality of this paper.

REFERENCES

Abell T., 2011, MNRAS, 413, 271
Agertz O. et al., 2007, MNRAS, 380, 963
Anders E., Grevesse N., 1989, Geochim. Cosmochim. Acta, 53, 197
Arnaud K. A., 1996, in Jacoby G. H., Barnes J., eds, ASP Conf. Ser. Vol. 101, Astronomical Data Analysis Software and Systems V. Astron. Soc. Pac., San Francisco, p. 17
Balsara D., 1995, J. Comput. Phys., 121, 357
Berger M. J., Colella P., 1989, J. Comput. Phys., 82, 64
Bianconi M., Ettori S., Nipoti C., 2013, MNRAS, 434, 1565
Biffi V., Dolag K., Böhringer H., 2011, MNRAS, 413, 573
Biffi V., Dolag K., Böhringer H., Lemson G., 2012, MNRAS, 420, 3545
Biffi V., Dolag K., Böhringer H., 2013a, Astron. Nachr., 334, 317
Biffi V., Dolag K., Böhringer H., 2013b, MNRAS, 428, 1395
Biffi V., Sembolini F., De Petris M., Valdarnini R., Yepes G., Gottlöber S., 2014, MNRAS, 439, 588
Böhringer H. et al., 2010, A&A, 514, A32
Borgani S., Kravtsov A., 2011, Adv. Sci. Lett., 4, 204
Buote D. A., Tsai J. C., 1995, ApJ, 452, 522
Cha S.-H., Inutsuka S.-I., Nayakshin S., 2010, MNRAS, 403, 1165
Dolag K., Jubelgas M., Springel V., Borgani S., Rasia E., 2004, ApJ, 606, L97
Ettori S. et al., 2013, preprint (arXiv:e-prints). Available at: http://adsabs.harvard.edu/abs/2013arXiv1306.2322E
Fang T., Humphrey P., Buote D., 2009, ApJ, 691, 1648
Fryxell B. et al., 2000, ApJS, 131, 273
Fujita Y., 2005, ApJ, 631, L17

Fujita Y., Matsumoto T., Wada K., 2004, ApJ, 612, L9

García-Senz D., Cabezón R. M., Escartín J. A., 2012, A&A, 538, A9

Gaspari M., Churazov E., 2013, A&A, 559, A78

Gaspari M., Churazov E., Nagai D., Lau E. T., Zhuravleva I., 2014, A&A, 569A, 15

Heß S., Springel V., 2010, MNRAS, 406, 2289

Hopkins P. F., 2014, preprint (arXiv:e-prints). Available at: http://adsabs.harvard.edu/abs/2014arXiv1409.7395H

Hu C.-Y., Naab T., Walch S., Moster B. P., Oser L., 2014, MNRAS, 443, 1173

Inogamov N. A., Sunyaev R. A., 2003, Astron. Lett., 29, 791

Inutsuka S.-I., 2002, J. Comput. Phys., 179, 238

Junk V., Walch S., Heitsch F., Burkert A., Wetzstein M., Schartmann M., Price D., 2010, MNRAS, 407, 1933

Khokhlov A. M., 1998, J. Comput. Phys., 143, 519

Kitsionas S. et al., 2009, A&A, 508, 541

Kravtsov A. V., Borgani S., 2012, ARA&A, 50, 353

Lau E. T., Kravtsov A. V., Nagai D., 2009, ApJ, 705, 1129

McCarthy I. G., Le Brun A. M. C., Schaye J., Holder G. P., 2014, MNRAS, 440, 3645

McNally C. P., Lyra W., Passy J.-C., 2012, ApJS, 201, 18

Markevitch M., Vikhlinin A., 2007, Phys. Rep., 443, 1

Mitchell N. L., McCarthy I. G., Bower R. G., Theuns T., Crain R. A., 2009, MNRAS, 395, 180

Mohr J. J., Fabricant D. G., Geller M. J., 1993, ApJ, 413, 492

Monaghan J. J., 1997, J. Comput. Phys., 136, 298

Morris J. P., Monaghan J. J., 1997, J. Comput. Phys., 136, 41

Morrison R., McCammon D., 1983, ApJ, 270, 119

Murante G., Borgani S., Brunino R., Cha S.-H., 2011, MNRAS, 417, 136

Nagai D., Lau E. T., Avestruz C., Nelson K., Rudd D. H., 2013, ApJ, 777, 137

Nandra K. et al., 2013, preprint (arXiv:e-prints). Available at: http://adsabs.harvard.edu/abs/2013arXiv1306.2307N

Norman M. L., Bryan G. L., 1999, in Miyama S. M., Tomisaka K., Hanawa T., eds, Astrophysics and Space Science Library, Vol. 240, Numerical Astrophysics. Springer-Verlag, Berlin, p. 19

O'Hara T. B., Mohr J. J., Bialek J. J., Evrard A. E., 2006, ApJ, 639, 64

Planelles S., Borgani S., Fabjan D., Killedar M., Murante G., Granato G. L., Ragone-Figueroa C., Dolag K., 2014, MNRAS, 438, 195

Power C., Read J. I., Hobbs A., 2014, MNRAS, 440, 3243

Price D. J., 2008, J. Comput. Phys., 227, 10040

Price D. J., 2012a, J. Comput. Phys., 231, 759

Price D. J., 2012b, MNRAS, 420, L33

Rasia E. et al., 2014, ApJ, 791, 13

Read J. I., Hayfield T., 2012, MNRAS, 422, 3037

Read J. I., Hayfield T., Agertz O., 2010, MNRAS, 405, 1513

Rebusco P., Churazov E., Sunyaev R., Böhringer H., Forman W., 2008, MNRAS, 384, 1511

Roediger E., Brüggen M., Simionescu A., Böhringer H., Churazov E., Forman W. R., 2011, MNRAS, 413, 2057

Roediger E., Kraft R. P., Forman W. R., Nulsen P. E. J., Churazov E., 2013a, ApJ, 764, 60

Roediger E., Kraft R. P., Nulsen P., Churazov E., Forman W., Brggen M., Kokotanekova R., 2013b, MNRAS, 436, 1721

Rosswog S., 2009, New Astron. Rev., 53, 78

Saitoh T. R., Makino J., 2013, ApJ, 768, 44

Schuecker P. F. A., Miniati F., Böhringer H., Briel U. G., 2004, A&A, 426, 387

Sijacki D., Vogelsberger M., Kereš D. S. V., Hernquist L., 2012, MNRAS, 424, 2999

Smith R. K., Brickhouse N. S., Liedahl D. A., Raymond J. C., 2001, ApJ, 556, L91

Springel V., 2010a, ARA&A, 48, 391

Springel V., 2010b, MNRAS, 401, 791

Springel V., Hernquist L., 2002, MNRAS, 333, 649

Sunyaev R. A., Norman M. L., Bryan G. L., 2003, Astron. Lett., 29, 783

Tasker E. J., Brunino R., Mitchell N. L., Michielsen D., Hopton S., Pearce F. R., Bryan G. L., Theuns T., 2008, MNRAS, 390, 1267

Teyssier R., 2002, A&A, 385, 337

Valcke S., de Rijcke S., Rödiger E., Dejonghe H., 2010, MNRAS, 408, 71

Valdarnini R., 2006, New Astron., 12, 71

Valdarnini R., 2011, A&A, 526, A158 (V11)

Valdarnini R., 2012, A&A, 546, A45

Wadsley J. W., Veeravalli G., Couchman H. M. P., 2008, MNRAS, 387, 427

ZuHone J. A., Markevitch M., Johnson R. E., 2010, ApJ, 717, 908

APPENDIX A: CLUSTER GLOBAL TEMPERATURES

In Tables A1 and A2, we report the global mass-weighted ($T_{\rm mw}$) temperatures of the clusters in the sample (referring, respectively, to adiabatic and cooling runs), for the regions enclosed within R_{200} and R_{2500}.

In particular, we choose to focus on one single viscosity scheme, the AV$_2$ run, and rather compare the standard NOAC implementation of SPH against the AC modification. The effects on the thermal properties of the ICM discussed in Section 5 are also reflected in the differences for the global temperatures.

Table A1. Cluster temperatures for both standard NOAC and AC runs (with AV$_2$ viscosity scheme) – adiabatic runs (ar2).

Index	$T_{200,\rm mw}$ (keV) NOAC/AC	$T_{2500,\rm mw}$ (keV) NOAC/AC
1	4.01/4.15	5.02/6.26
5	1.82/1.90	2.25/2.68
11	4.20/4.32	5.35/5.85
13	3.13/3.24	3.84/4.11
16	1.75/1.92	2.14/2.55
19	4.49/4.58	5.51/6.28
105	0.98/1.02	1.24/1.32
110	1.35/1.34	1.71/1.71

Table A2. Same as Table A1 but for radiative runs (cr2).

Index	$T_{200,\rm mw}$ (keV) NOAC/AC	$T_{2500,\rm mw}$ (keV) NOAC/AC
1	4.20/4.47	5.74/6.42
5	2.08/2.19	2.92/3.09
11	4.58/4.79	6.55/7.11
13	3.37/3.52	4.66/5.03
16	1.94/2.11	2.70/3.20
19	4.81/4.89	6.47/7.01
105	1.07/1.14	1.49/1.60
110	1.49/1.51	2.13/2.26

This paper has been typeset from a TEX/LATEX file prepared by the author.